Plasmonic nanoparticle arrays fabricated and modified by energetic ions for chemical sensors

Kazuhiro Kawaguchi

Graduate School of Science and Technology

Kyoto Institute of Technology

2013

Contents

Chapter 1

General introduction

1.1. Optical property of noble-metal nanoparticles

In recent years, metal nanoparticles (NPs) have been the object of continuously growing interest due to their optical properties. In particular, silver (Ag) and gold (Au) NPs with sizes in the range of 10 to 100 nm are resonantly of light. At frequency of the resonance, referred to as plasmon resonance, the absorption cross-section can be several times higher than that expected from the geometrical cross-section of the particle. Noble-metal NPs can support localized surface plasmon resonance (LSPR) when the incident photon frequency is resonant with the collective oscillation of the conduction electrons confined in the volume of the NPs (Fig. 1.1). The simplest type of LSPR is a dipolar LSPR, which can be seen in the limit of the particle's diameter, d, being much smaller than the wavelength of the incident light, λ ($d << \lambda$). Moreover, in this size range only limited scattering of the incident light occurs [1−8].

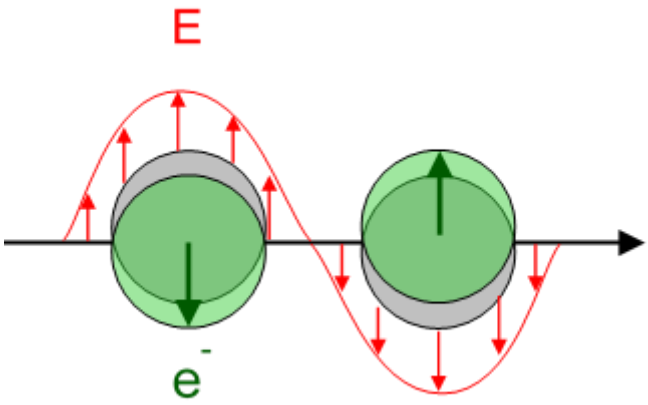

Fig. 1.1: Schematic illustration of a localized surface plasmon of a metal sphere showing the displacement of the electron charge cloud relative to the ion core [9].

Optical extinction is attenuation of light by scattering and absorption as it traverses a particulate medium. In homogeneous media, the dominant attenuation mechanism is usually absorption. The extinction cross section C_{ext} is the sum of absorption and scattering cross sections given by

$$C_{ext} = C_{abs} + C_{sc} . \quad (1.1)$$

The optical extinction cross sections of Ag and Au nanoparticles with the size 10−60 nm were simulated by using MQAggr software [10]. The results shown in Figs. 1.2 and 1.3 indicate that the absorption cross sections are dominant for their extinction cross sections except for the large size (60 nm). Therefore, the optical extinction is nearly equal to the optical absorption for the NPs with size ≤ 30 nm.

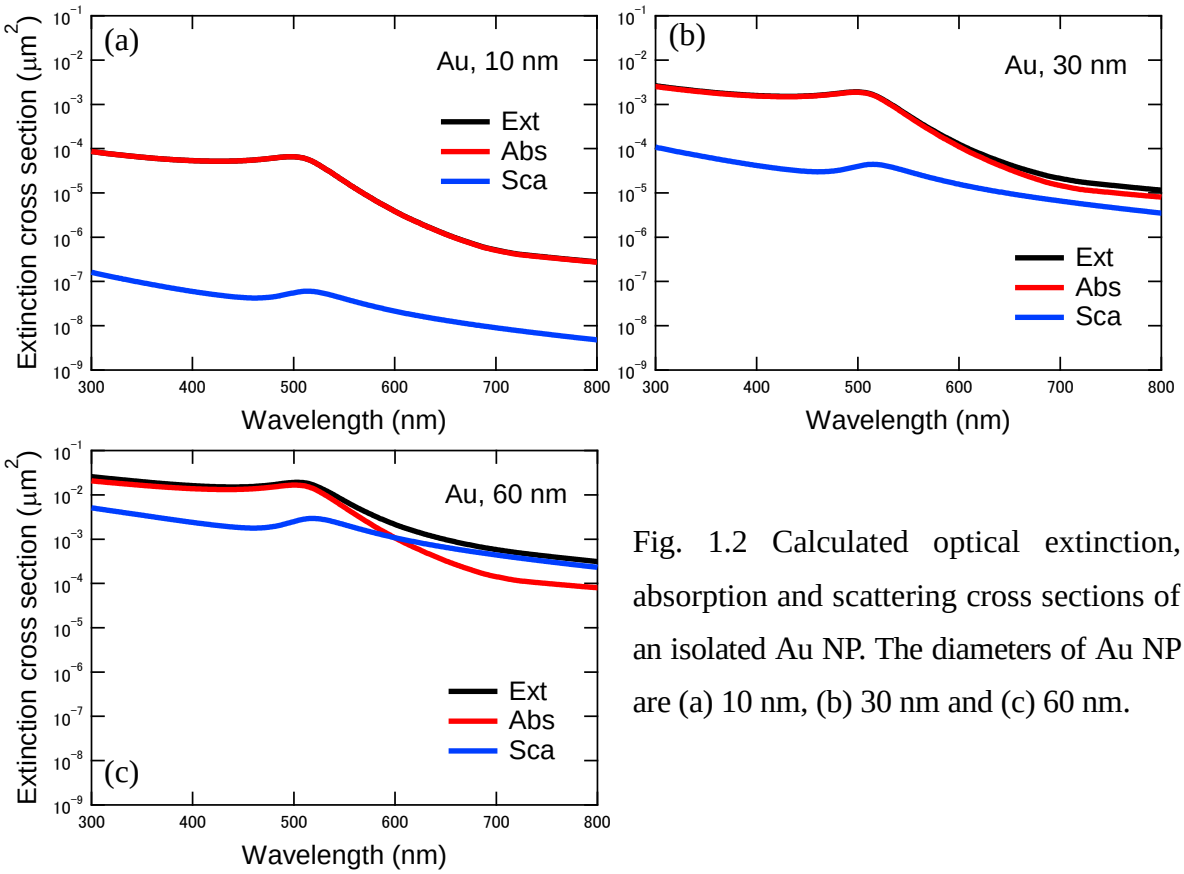

Fig. 1.2 Calculated optical extinction, absorption and scattering cross sections of an isolated Au NP. The diameters of Au NP are (a) 10 nm, (b) 30 nm and (c) 60 nm.

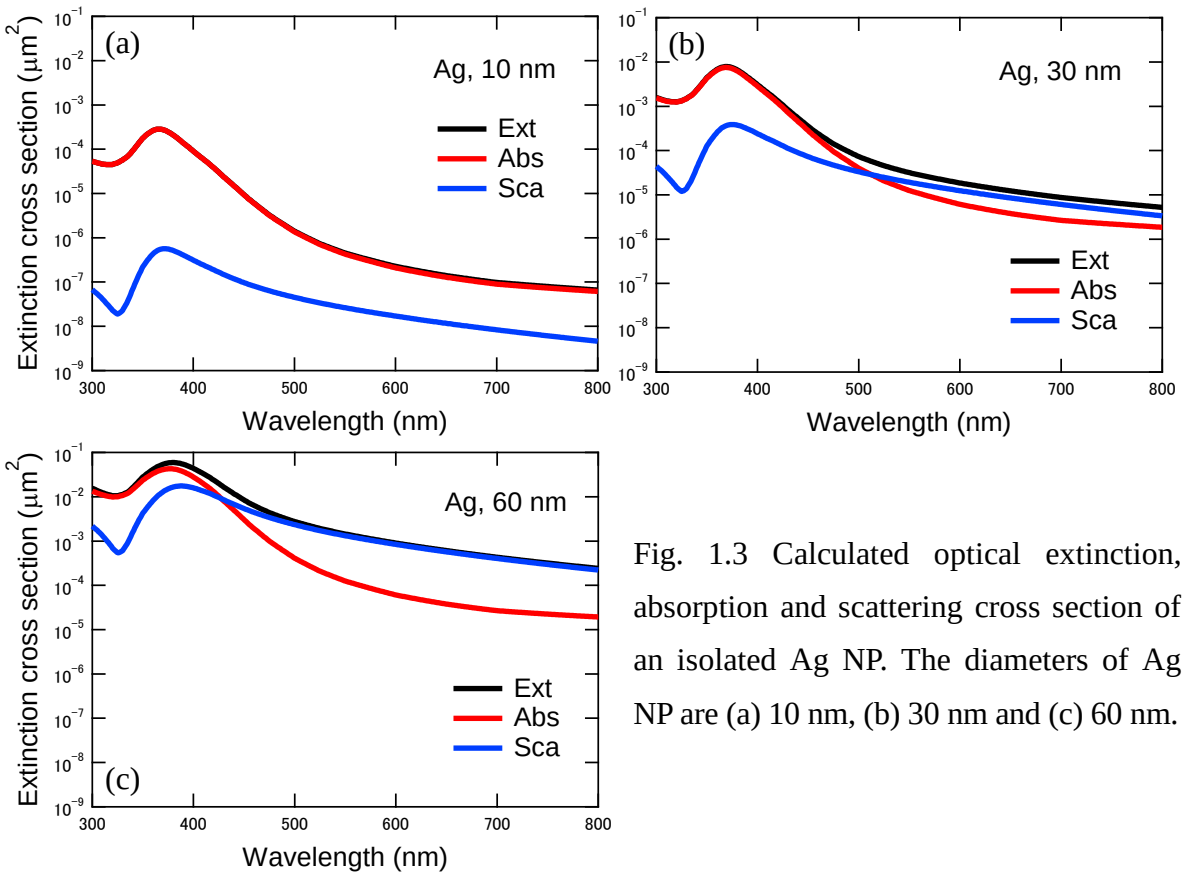

Fig. 1.3 Calculated optical extinction, absorption and scattering cross section of an isolated Ag NP. The diameters of Ag NP are (a) 10 nm, (b) 30 nm and (c) 60 nm.

The plasmon resonance for metal nanospheres with diameters between 5 and 50 nm is nearly independent of size. This is because the gradient of the real part of the dielectric function, at the plasmon resonance, is large, and the size-dependent shift in the plasmon resonance is inversely proportional to this gradient [11]. For particles smaller than about 5 nm, scattering of electrons off the surface [7, 12] causes a significant decrease in the resonance amplitude, plus a broadening and slight blue-shift in its position. For particles larger than about 50 nm, there is also a shift in the resonance peak since higher-order terms begin to contribute to the extinction, but with an attendant loss of spectral selectivity.

The Mie theory [13] allows one to calculate the exact optical response of the system by solving the Maxwell equations in the medium, provided that the clusters are spherical and isolated from each other. The Mie theory predicts that the position and width of the LSPR are closely related to particle diameter *D* as shown below [14]:

$$\frac{\lambda_{\mathrm{p}}^2}{\Delta\lambda} = \frac{\upsilon_{\mathrm{F}}}{\pi c} \cdot \frac{1}{D}, \tag{1.2}$$

where $\Delta\lambda$ is FWHM and λ_{p} the peak wavelength of LSPR extinction band, υ_{F} the Fermi velocity of the electron in bulk metal, *c* the velocity of light and *D* the diameter of metal nanoparticles. The calculated optical extinction cross sections for isolated Au and Ag NPs in air are shown in Fig. 1.4. The diameter of Au and Ag NPs was changed from 10 to 60 nm. From the figures, one

can find that the differences in peak position and width among these size are not so large both for Au and Ag NPs.

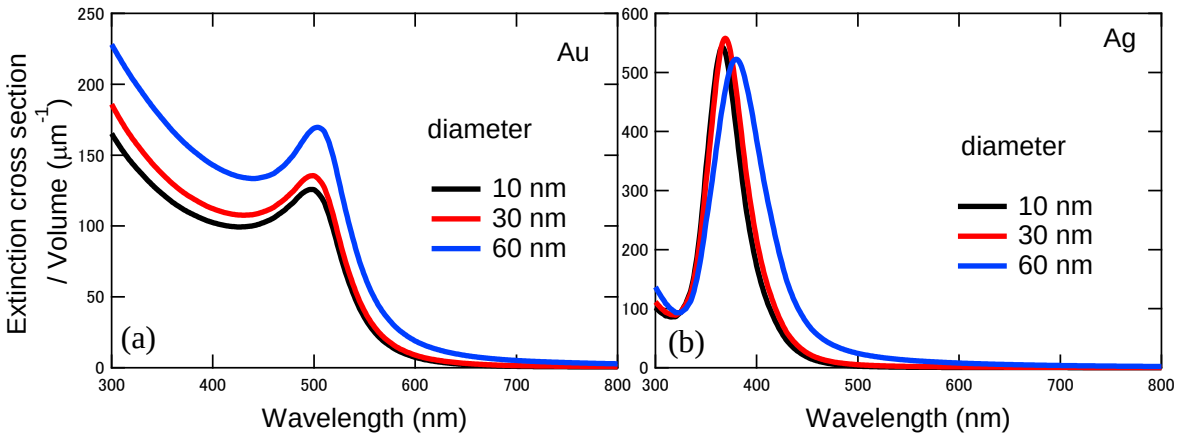

Fig. 1.4: Calculated optical extinction cross sections of isolated (a) Au and (b) Ag NPs with diameters of 10−60 nm, normalized by their volume.

Next, the author considers the optical extinction by a single NP coated with a dielectric. Here also the simulation of such NPs is helpful to understand the effect of the dielectric coating on an extinction spectrum. Fig. 1.5 shows the dependence of the extinction cross section of PET (Polyethylene terephthalate) coated Au sphere in air on the PET thickness. The refractive index of PET is 1.6, much larger than that of air (1.0). It can be found that peak becomes intense and the resonance position shifts toward longer wavelength as the PET thickness increases.

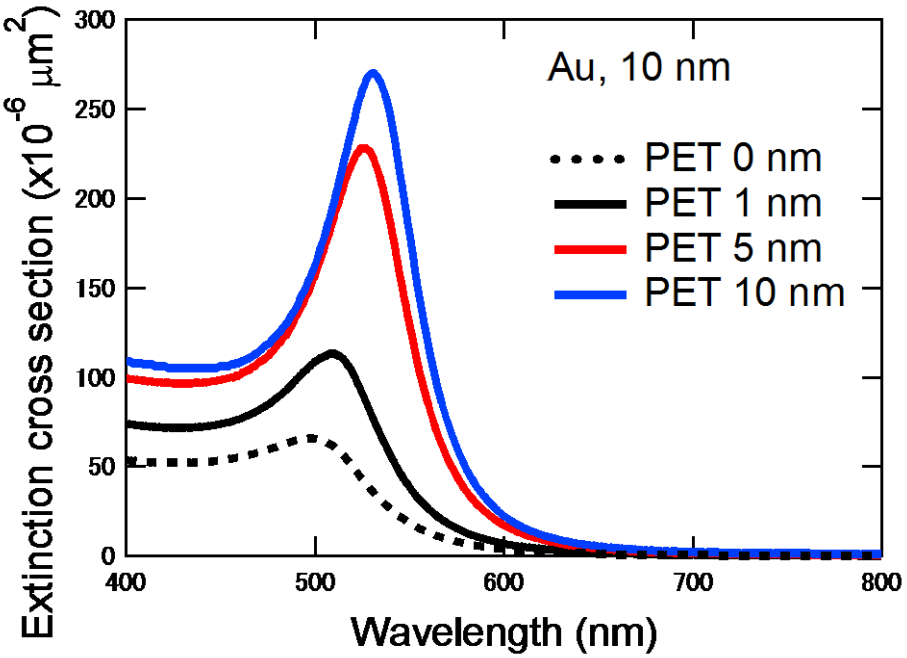

Fig. 1.5: Calculated optical extinction cross sections of an isolated Au NPs coated with a PET film of thickness 1−10 nm. The diameter of the Au NP is fixed at 10 nm.

In the previous paragraphs, NP size and refractive index dependences are described for an isolated single NP. Considering plasmonic applications like this study, however, the optical properties of multi-particle system such as a NP aggregate and NP array should be presented. There are two key parameters, the inter-particle distance and geometry, which determine optical properties of an aggregate. In the optical extinction spectrum, resonant wavelength and intensity are very sensitive to the inter-particle distance between two NPs. As shown in Fig. 1.6, the extinction cross section is greatly enhanced as the inter-particles distance

decreases. In addition, red shift of resonance wavelength is observed as two NPs approach each other. In Fig. 1.7, some computed spectra are shown for a linear quartet, T-shaped and square Au aggregates. Geometry of aggregates is found to be an important factor to control plasmonic properties of NPs. Optical properties of NP aggregate also depend on other factors including a crystal form, shape, filling factor, and so on. The most realistic arrangement of a NP aggregate consists of more or less densely packed single NPs plus aggregates with various neighbor distances, coordination numbers, size and shape, which for their part, again are packed more or less closely together. In my opinion, it is very hard or impossible to prepare a NP aggregate by bottom-up way to exactly control its optical property because of large number of parameters considered. Additional modification of a plasmonic property of self-organized aggregates or arrays by a certain method is an easier and reliable approach to obtain a desired one.

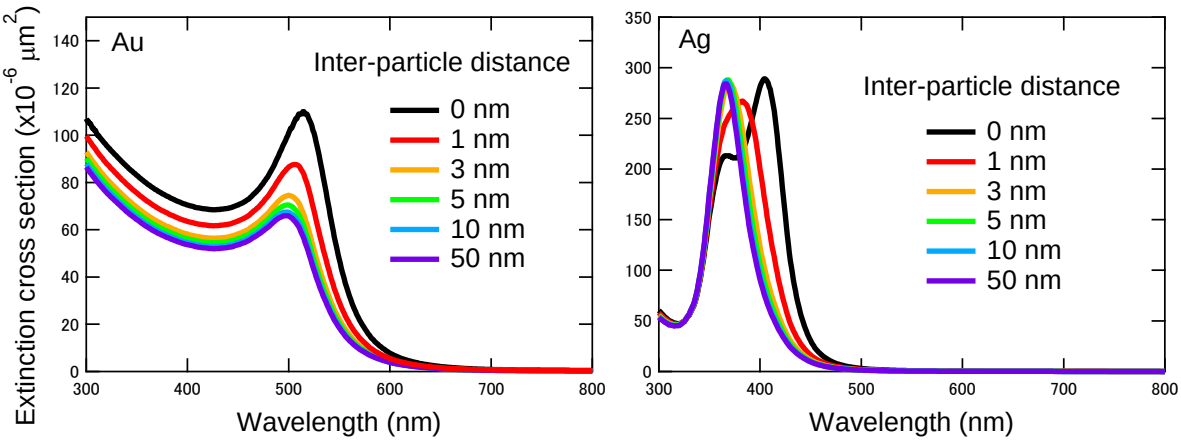

Fig. 1.6: Calculated optical extinction cross sections of two Au and Ag NPs with diameter of 10 nm. The calculation is performed for various inter-particle distances between the two NPs.

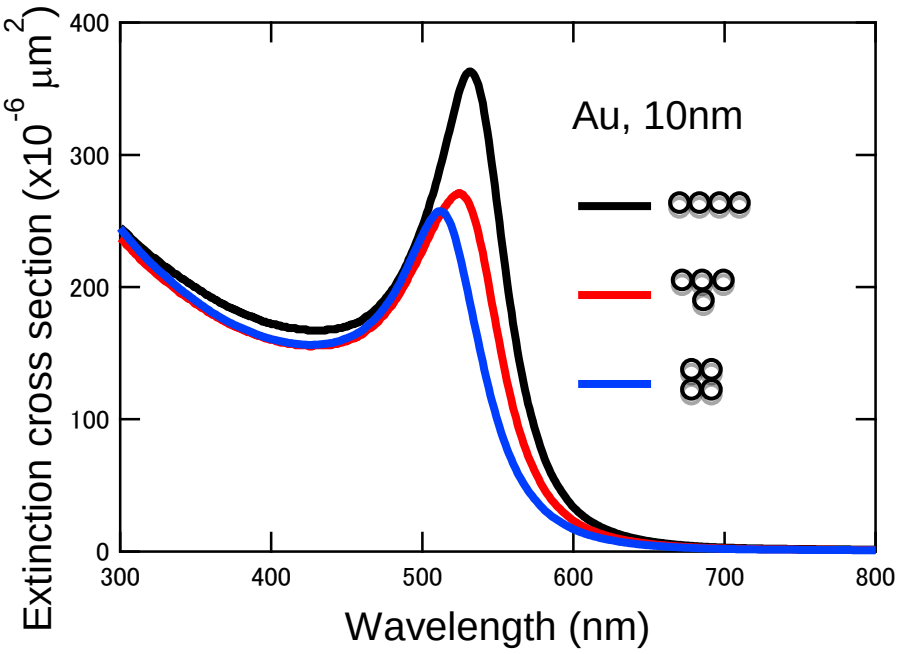

Fig. 1.7: Calculated optical extinction cross sections of proximity four Au NPs with diameter of 10 nm. The calculation is performed for different geometries of linear quartet, T-shaped and square aggregates

1.2. Plasmonic sensing by using Ag and Au nanoparticle aggregates

Fundamentals and a variety of applications for plasmonic sensing with Ag and Au nanostructures have been reviewed in literature by Stewart et al. [15]. Here some useful applications and problems concerning with plasmonic sensing are introduced on the basis of their paper.

The refractive index sensitivity of Ag NP arrays has been exploited in sensing applications where peak shifts were used to detect adsorption at the NP surfaces [16−21]. The

experimentally measured peak shifts were monitored in conjunction with a simple mathematical formalism developed for flat film SPR spectroscopy to quantitatively evaluate sample concentrations [22]. This procedure enabled one to quantitatively detection Concanavalin A [19], streptavidin [16], and anti-biotin [18]. In a notable example, triangular NP arrays were fabricated to detect biomarkers for Alzheimer's disease in both synthetic and human patient samples [17]. In that work, synthetic amyloid-β-derived diffusible ligands (ADDL) were detected at femto-molar concentrations in an elegant way [17].

The sensitivity of these types of measurements is enhanced if the molecular resonance of the analyte overlaps with the intrinsic LSPR of the NPs or if the analyte is labeled with a marker that has a resonance that overlaps with the intrinsic LSPR of the NPs [23,24]. One of the advantages of using plasmonic nanostructures for sensing is their relatively small footprints−one that is more amenable to miniaturization than flat film SPR detection. For example, LSPR sensing has been demonstrated at the single-NP level using spherical (Ag [25] and Au [26]), triangular (Ag) [27] and cubic (Ag) NPs [28]. Scattering-based spectroscopies must be used to characterize the optical properties of single NPs since the absorbance of individual NPs is close to the shot noise-governed limit of detection. McFarland and Van Duyne [29], for example, have shown that a LSPR peak shift of ~40 nm occurs upon adsorption of ~100 zepto-moles of

1-hexadecanethiol to a single triangular Ag NP. This high sensitivity and small transducer size suggests that even single NPs could be useful for the analysis of precious or limited-volume samples.

There is another method called transmission LSPR (T-LSPR or T-SPR) spectroscopy developed by Rubinstein [30]. In this method one measures the changes in the LSPR peak intensity and position for discontinuous Au or Ag films upon analyte adsorption, which is monitored in transmission mode using a conventional spectrophotometer. Discontinuous and random island films for this plasmonic measurement are prepared by direct evaporation of an ultrathin (nominal thickness $\leq$10 nm) layer of the desired metal onto a transparent substrate such as quartz. Random Au island films, for example, display a LSPR extinction peak at 550−800 nm, depending on the island morphology, which in turn is determined by the evaporation conditions and post-deposition treatment. An optimization of such conditions is just related to my present work, as will be shown in the fourth chapter of this thesis. Rubinstein and co-workers demonstrated the potential of this method by measuring changes in the position and intensity of the LSPR extinction band that result from the attaching of various molecules to Au islands [30−34].

As has been pointed out by Stewart et al. [15], the instability of simple T-LSPR

sensors is a source of concern. Changes in the optical properties of metal island films due to morphological changes occurring upon immersion in organic solvents and aqueous solutions has been noted to appreciably introduce uncertainties into NP-based sensing measurements. To obtain metal island films with stable and reproducible optical properties, new design schemes for stabilizing the structures of the evaporated film have been devised. The most useful and realizable procedure consists of depositing an ultrathin silica layer (1.5 nm thick) on the metal island film by a sol-gel procedure [34]. A sputter deposition technique, as has been used in this work, can be an alternative method to prepare such a thin layer.

1.3. Fundamentals of analytical methods used in this study

Two analytical methods, optical absorption spectroscopy and Rutherford backscattering spectrometry, were mainly utilized throughout this work. Fundamentals of these analyses are described briefly.

1.3.1. Optical absorption spectroscopy

Optical absorption spectroscopy usually referred to as ultraviolet and visible

(UV-Vis) absorption spectroscopy is the measurement of the attenuation of a beam of light after it passes through a sample or after reflection from a sample surface. Absorption measurements can be at a single wavelength or over an extended spectral range. Ultraviolet and visible light are energetic enough to promote outer electrons to higher energy levels, and UV-Vis spectroscopy is usually applied to molecules or inorganic complexes in solution. The UV-Vis spectra have broad features that are of limited use for sample identification but are very useful for quantitative measurements. Since the UV-Vis range spans the range of human visual acuity of approximately 400−750 nm, UV-Vis spectroscopy is useful to characterize the absorption, transmission, and reflectivity of a variety of technologically important materials, such as pigments, coatings, windows, and filters. This more qualitative application usually requires recording at least a portion of the UV-Vis spectrum for characterization of the optical or electronic properties of materials.

In single-beam UV-Vis absorption spectroscopy, obtaining a spectrum requires manually measuring the transmittance of the sample and solvent at each wavelength. The dual-beam design greatly simplifies this process by simultaneously measuring P and P_0 of the sample and reference cells, respectively (see Fig. 1.8). Most spectrometers use a mirrored rotating chopper wheel to alternately direct the light beam through the sample and reference

cells. The detection electronics or software program can then manipulate the P and P_0 values as the wavelength scans to produce the spectrum of absorbance or transmittance as a function of wavelength.

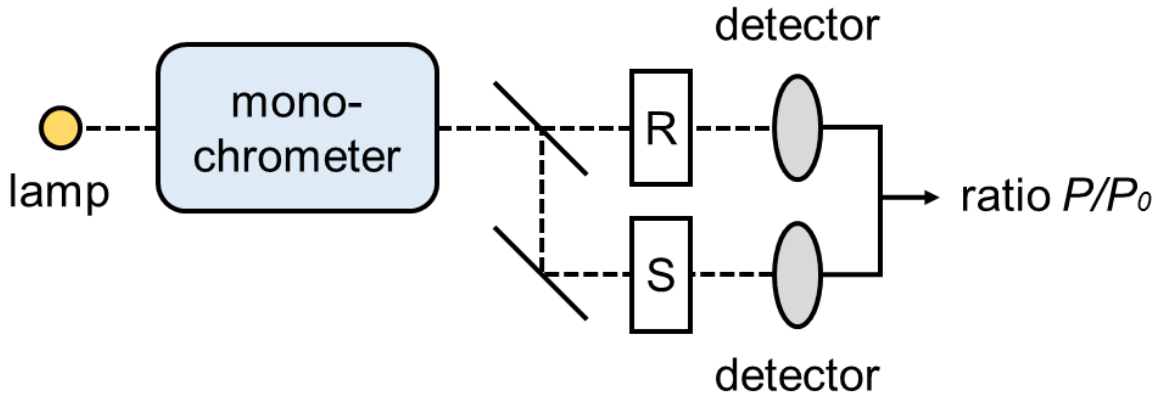

Fig 1.8: Schematic of a dual-beam UV-vis spectrophotometer.

1.3.2. Rutherford backscattering spectrometry

Rutherford backscattering spectrometry (RBS) is a non-destructive techniques for quantitative analysis of elemental composition, thickness and depth profile of material surfaces. In RBS, the primary ion is usually H^+ or He^+, whose energy ranges from about several hundred keV to MeV [35]. This primary ion beam impinges on a target, and the energies and numbers of backscattered ions are analyzed with a detector. Because of its quantitative reliability, RBS is often used as a standard tool for other surface analytical techniques. In the following sections, four physical quantities of RBS, (1) kinematic factor, (2) scattering cross section, (3) stopping

power, (4) strugglings, will be described in detail.

(1) *Kinematic factor*

As mentioned above, a beam of monoenergetic light ions is incident on a solid target and the energy spectrum of particles backscattered from target atoms into a fixed angle is measured. The energy of the scattered particle depends on the masses of the projectile and the target atom, which gives elemental information of analyte. Here one considers the collision between two particles. The energy transfer in an elastic collision between the two particles can be expressed by applying the principles of conservation of energy and momentum. The projectile (mass M_1) has an incident energy E_0 and the target (mass M_2) is initially at rest.

The ratio K, referred to as kinematic factor, of the scattering energy E_1 to the incident energy E_0 for $M_1 < M_2$ can be given by

$$K \equiv \frac{E_1}{E_0} = \left[\frac{M_1 \cos\theta + \sqrt{M_2^{\,2} - M_1^{\,2} \sin^2\theta}}{M_1 + M_2} \right]^2 . \qquad (1.3)$$

The scattering angle θ is defined as the angle between the projectile incident direction and the scattered direction. For a given M_1, E_0, and θ, the mass M_2 of the target atom is uniquely determined from Eq. (1.3) by measuring the energy E_1. For example, the kinematic factor K is calculated to be 0.862 for the ^{4}He-Ag collision in the case of $\theta = 165°$.

(2) *Scattering cross section*

Scattering cross section σ can be calculated from the force that acts during the collision between the projectile and the target atom. This leads to the capability of quantitative analysis of atomic composition. Using the differential scattering cross section $d\sigma/d\Omega$, one can estimate how frequently such a collision actually takes place and ultimately the scattering yield at a certain angel θ. If the collision events occur according to the pure Coulomb scattering, the differential scattering cross section is given by the Rutherford formula [36],

$$\frac{d\sigma}{d\Omega} = \left(\frac{Z_1 Z_2 e^2}{4E_0} \right)^2 \times \frac{4\left[\sqrt{M_2{}^2 - M_1{}^2 \sin^2\theta} + M_2 \cos\theta \right]^2}{M_2 \sin^4\theta \sqrt{M_2{}^2 - M_1{}^2 \sin^2\theta}}, \tag{1.4}$$

where Z_1 and Z_2 are the atomic numbers of the incident particle and target atoms, respectively. For a target of a thin film with a thickness of t, the yield Y of particles detected by a finite acceptance solid angle $\Delta\Omega$ at a scattering angle θ can be written as,

$$Y = N \cdot t \times \frac{d\sigma}{d\Omega} \times \frac{\Delta\Omega \cdot Q}{\cos\alpha}, \tag{1.5}$$

where Q stands for the number of incident ions impinging on the target, N the atomic density of the target and α the incident angle schematically shown in Fig. 1.9.

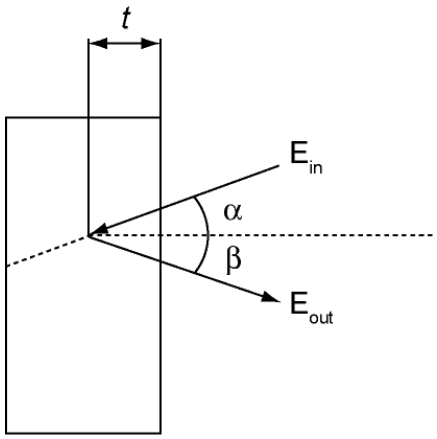

Fig. 1.9: Schematic drawing of the scattering geometry.

(3) *Stopping power*

The stopping power of a material for a particular incident ion is usually defined as the energy loss per distance traveled in the material, denoted as *dE/dx* (usually given in eV/ Å). There are two mechanisms responsible for the energy loss of the projectile: nuclear stopping which originates from a multitude of small-angle collisions of the projectile with the atomic nuclei of the target, and the electronic stopping which comes from inelastic collisions with the electron clouds surrounding each target atom.

Additionally the stopping cross section *S* [eV/(atoms/cm^2)] is defined as the energy loss/atoms/cm^2 (areal density) of material traversed. This quantity is independent of the volume density of the material. The relation between stopping power and stopping cross section is represented by

$$S = \frac{1}{N}\frac{dE}{dx}, \tag{1.6}$$

where N is the atomic density (atoms/cm^3). Values of ion stopping cross sections in all elements are available from an extensive study based on semi-empirical fitting of experimental data [37].

The energy, E_{out}, of the ion emerging from the target surface after scattering at a depth t can be given by,

$$E_{out} = K\left[E_{in} - \frac{t}{|\cos\alpha|}\cdot\left(\frac{dE}{dx}\right)_{in}\right] - \frac{t}{|\cos\beta|}\cdot\left(\frac{dE}{dx}\right)_{out} \tag{1.7}$$

where α and β are incident angle and exit angle which are shown in Fig. 1.9. $(dE/dx)_{in}$ and $(dE/dx)_{out}$ refer to the stopping power of inward path and outward path, respectively. This equation shows that the depth t where the scattering occurred can be calculated from the detected ion energy. This calculation will be presented in Chapter 2.

As described so far, energy and numbers of detected particle at a scattering angle θ gives information on concentration and depth of target atoms. Therefore, RBS serves compositional depth profile of material surface, without using sputtering erosion process.

(4) *Straggling*

When a beam of charged particles penetrates matter, the slowing down is accompanied by a spreading of the beam energy. This phenomenon is called energy straggling. It is due to statistical fluctuations in the number of collision processes. As a result, identical energetic particles, which all have the same initial energy, do not have exactly the same energy after pass even through an identical thickness *t* of a homogeneous medium. When the energy transfers to target electrons in the individual collisions are small compared to the width of the energy loss distribution, the distribution is close to a Gaussian. In the limit of high ion velocity, the energy loss is dominated by electronic excitations. In this region straggling is almost independent of projectile velocity. In the Gaussian distribution regime a simple expression was derived by Bohr [38]. The standard deviation Ω of the energy distribution of ions passing through a medium of thickness *t* is expressed as

$$\Omega_B^{\,2} = 4\pi Z_1^{\,2} Z_2 e^4 N t \tag{1.8}$$

This process leads to a limitation in the ultimate mass and depth resolution for RBS.

1.4. Outline of this thesis

As seen in the early part of this section, plasmonic NPs made of Ag and Au exhibit unique optical properties due to LSPR in the visible wavelength range. A plasmonic sensor is one of the most useful applications of such nanoparticles. In this thesis, energetic ion processes including ion implantation, sputtering and plasma exposure were utilized to fabricate and modify Ag or Au NP arrays for sensing applications.

The second chapter of this thesis, corresponding to my publication list No. 1, describes the method to fabricate well-ordered and densely arranged Ag NPs embedded in a thermally grown SiO_2 by implanting with 350 keV silver ions. In the third chapter, a sputter deposition technique to prepare densely arranged Ag NP array which posses a nice plasmonic characteristic is presented and then plasma exposure is applied for cleaning the NP arrays, which corresponds to my publication list No. 2. A drastic change in LSPR characteristics of plasma treated Ag and Au NP can be seen. Finally, the fourth chapter, corresponding to my publication list No.3, deals with the plasmonic sensing ability of Au NPs, fabricated on SiO_2 by a sputter deposition technique, for dilute cyclohexane.

References

[1] M. Quinten & U. Kreibig, Surf. Sci., 1986, **172**, 557.

[2] C. F. Bohren & D. R. Huffman: *Absorption and Scattering of Light by Small Particles* (Wiley, New York, 1998).

[3] S. Link & M. A. El-Sayed, Inter. Rev. Phys. Chem. 2000, **19**, 409.

[4] K. L. Kelly, E. Coronado, L. L. Zhao & G. C. Schatz, J. Phys. Chem. B 2003, **107**, 668.

[5] C. J. Murphy et al., J. Phys. Chem. B 2005, **109**, 13857.

[6] C. J. Murphy, A. M. Gole, S. E. Hunyadi & C. J. Orendorff, Inorg. Chem. 2006, **45**, 7544.

[7] P. Mulvaney, Langmuir 1996, **12**, 788.

[8] J. Perez-Juste, I. Pastoriza-Santos, L. M. Liz-Marzan & P. Mulvaney, Coordin. Chem. Rev. 2005, **249**, 1870

[9] K. A. Willets, R. P. Van Duyne, Ann. Rev. Phys. Chem. 2006, **58**, 267.

[10] M. Quinten, Wissenschaftlich-technische.

[11] M. G. Blaber, N. Harris, M. J. Ford & M. B. Cortie. in 2006 International Conference on Nanoscience and Nanotechnology (eds. C. Jagadish and G. Q. M. Lu,) 556 (IEEE Publishing Co, Piscataway, USA, Brisbane, 2006).

[12] M. M. Alvarez et al., J. Phys. Chem. B 1997, **101**, 3706.

[13] G. Mie, Ann. Phys. 1908, **25**, 377.

[14] D. Manikandan, S. Mohan, P. Magudaphy, K.G.M. Nair, Physica B 2003, **325**, 86.

[15] M. E. Stewart, C. R. Anderton, L. B. Thompson, J. Maria, S. K. Gray,J. A. Rogers, R. G. Nuzzo, Chem Rev. 2008, **108**, 494.

[16] A. J. Haes, R. P. Van Duyne, J. Am. Chem. Soc. 2002, **124**, 10596.

[17] A. J. Haes, L. Chang,W. L. Klein, R. P. Van Duyne, J. Am. Chem. Soc. 2005, **127**, 2264.

[18] J. C. Riboh, A. J. Haes, A. D. McFarland, C. R. Yonzon, R. P. Van Duyne, J. Phys. Chem. B 2003, **107**, 1772.

[19] C. R. Yonzon, E. Jeoung, S. Zou, G. C. Schatz, M. Mrksich, R. P. Van Duyne, J. Am. Chem. Soc. 2004, **126**, 12669.

[20] A. J. Haes, S. Zou, G. C. Schatz, R. P. Van Duyne, J. Phys. Chem. B 2004, **108**, 6961.

[21] A. J. Haes, S. Zou, G. C. Schatz, R. P. Van Duyne, J. Phys. Chem. B 2004, **108**, 109.

[22] L. S. Jung, C. T. Campbell, T. M. Chinowsky, M. N. Mar, S. S. Yee, Langmuir 1998, **14**, 5636.

[23] J. Zhao, A. Das, X. Zhang, G. C. Schatz, S. G. Sligar, R. P. Van Duyne, J. Am. Chem. Soc. 2006, **128**, 11004.

[24] A. J. Haes, S. Zou, J. Zhao, G. C. Schatz, R. P. Van Duyne, J. Am. Chem. Soc. 2006, **128**, 10905.

[25] J. J. Mock, D. R. Smith, S. Schultz, Nano Lett. 2003, **3**, 485.

[26] G. Raschke, S. Kowarik, T. Franzl, C. Sonnichsen, T. A. Klar, J. Feldmann, A. Nichtl, K. Kurzinger, Nano Lett. 2003, **3**, 935.

[27] L. J. Sherry, R. Jin, C. A. Mirkin,G. C. Schatz, R. P. Van Duyne, Nano Lett. 2006, **6**, 2060.

[28] L. J. Sherry, S.-H. Chang, G. C. Schatz, R. P. Van Duyne, B. J. Wiley, X. Younan, Nano Lett. 2005, **5**, 2034.

[29] A. D. McFarland, R. P. Van Duyne, Nano Lett., 2003, **3**, 1057.

[30] G. Kalyuzhny, A.Vaskevich, M. A. Schneeweiss, I. Rubinstein, Chem. Eur. J. 2002, **8**, 3849.

[31] M. Lahav, A. Vaskevich, I. Rubinstein, Langmuir 2004, **20**, 7365.

[32] G. Kalyuzhny, M. A. Schneeweiss, A. Shanzer, A. Vaskevich, I. Rubinstein, J. Am. Chem. Soc. 2001, **123**, 3177.

[33] G. Kalyuzhny, A. Vaskevich, G. Ashkenasy, A. Shanzer, I. Rubinstein, J. Phys. Chem. B. 2000, **104**, 8238.

[34] I. Ruach-Nir, T. A. Bendikov, I. Doron-Mor, Z. Barkay, A. Vaskevich, I. Rubinstein, J. Am. Chem. Soc. 2007, **129**, 84.

[35] L. C. Feldman, J. W. Mayer, *Fundamentals of Surface and Thin Film Analysis* (North-Holland, Amsterdam, 1986).

[36] W. K. Chu, J. W. Mayer and M. A. Nicolet: *Backscattering Spectrometry* (Academic press, New York, 1978).

[37] J.F. Zirgler: *Helium Stopping Powers and Ranges in All Elemental Matter*, (Pergamon Press, New York, 1977).

[38] N. Bohr, Kgl. Danske Videnskab. Matt-Fys. Medd. 1948, **18**, 8.

Chapter 2

Well-ordered arranging of Ag nanoparticles in SiO_2/Si by ion implantation

2.1. Introduction

In this chapter, the author shows the method of preparing of Ag nanoparticle using ion implant. A nanometer-sized metallic particle, referred to as metallic nanoparticle, embedded in a transparent dielectric exhibits a large third-order nonlinear susceptibility with picoseconds response time, and going to be applied to nonlinear optical devices [1]. Further, embedded metallic nanoparticles (MNPs) are expected to be stable materials for surface enhanced Raman spectroscopy (SERS), because host materials protect MNPs from corrosion [2,3]. Various methods, including co-sputtering [4], sequential evaporation [5], sol-gel deposition [6] and ion implantation [7,8] are being used to fabricate MNPs in a matrix. Of these techniques ion implantation is very promising for wafer-scale fabrication of MNPs embedded in the near-surface region of a wide variety of substrates.

In most cases, the depth distribution of implanted atoms exhibits Gaussian-type profile as expected by computer simulation such as SRIM [9]. In the case of implantation of Ag ions into SiO_2 substrates at high fluences, typically 10^{16}–10^{17} ions/cm^2, Ag atoms implanted distribute abnormally even at room temperature [10−14], as confirmed by Rutherford backscattering spectrometry (RBS) with MeV-energy [15] which is mentioned in the previous chapter, due to thermally activated, stress-induced and damage-related diffusion. Arnold and Borders [10] showed non-Gaussian depth distribution of Ag atoms in lithia-alumina-silica glass

implanted with 275 keV-Ag^+ at 10^{16} ions/cm^2, depending on implantation temperature and ion current density. Matsunami and Hosono [11] found that the Ag depth profile in SiO_2 glass implanted with 150 keV-Ag^+ to fluences of $0.1-60\times10^{16}$ ions/cm^2 became narrower with increasing an Ag ion fluence, which means localization of Ag atoms during colloidal formation. Liu et al. [12,13] demonstrated that abnormal non-Gaussian depth profiles of Ag in single crystal SiO_2 implanted with 200 keV-Ag^+ to $0.5-6.7\times10^{16}$ ions/cm^2, characteristics of narrow width and an additional small peak, were associated with nanoparticles formed around projected range of Ag ions. Concerning with abnormal depth profiles, the synthesis of self-organized single layers (δ-layers) of Ag nanoparticles formed by ultra-low-energy ion implantation into thermally grown SiO_2 on Si (SiO_2/Si) [16] is rather unique and attractive for fabrication of single electron devices [17] as well as stable SERS substrates [2,3].

In the course of Ag ion implantation into SiO_2/Si, we observed unexpected depth profiles, depending on the thickness of SiO_2 top-layer. The Ag profile consists of multi components, at least, narrow one localized around projected range of Ag ions and broad one distributed throughout the SiO_2 layer. In some cases, Ag segregations at the surface region of SiO_2 and the SiO_2/Si interface have been clearly observed. In the present study, the Ag containing SiO_2 layers have been characterized with several tools, such as cross-sectional transmission electron microscopy (X-TEM), X-ray photoelectron spectroscopy (XPS), X-ray

diffraction (XRD) as well as RBS to examine the structure of Ag-implanted SiO_2/Si.

Practically, stability against oxidation [18−20] and sulfidation [21−23] of Ag nanoparticles in ambient conditions is of importance. In this work, XPS Auger parameter (AP) analysis [24] has been applied to explore the oxidation state of Ag nanoparticles formed by ion implantation into SiO_2/Si. The AP is essentially independent of sample charging and work function, applicable to a particular element in a dielectric material. Here summing the XPS binding energy and Auger electron kinetic energy together provide the AP [25]. Although Ag core-level binding energy (e.g. $3d_{5/2}$) does not show much shift from Ag^0 to Ag^+, the Ag^0 and Ag^+ Auger lines (e.g. $M_4N_{4,5}N_{4,5}$) show considerable shift and can be used for identification purposes. The APs of Ag, Ag_2O, AgO and Ag_2S were measured to be 726.0, 724.3, 724.2 and 724.8 eV, respectively [26].

2.2. Experimental methods

A 300 nm thick thermally grown SiO_2 layer on a (111) Si was used as a substrate. Additionally, a thicker SiO_2 film (~ 700 nm) was prepared. The SiO_2/Si substrate was implanted with 350 keV-Ag ions to a fluence of 10^{17} ions/cm^2 using a 400 kV ion implanter of at Takasaki Ion Accelerator for Radiation Application (TIARA) of JAEA, Takasaki. The

beam-current density was typically 4 μA/cm^2 and temperature measured on the substrate by using a thermocouple was as low as 430 K. Reduced beam current density (~ 0.6 μA/cm^2) was also used. The SiO_2 thickness was chosen to stop almost all the implanted Ag ions inside the SiO_2 layer. The Ag depth profiles were measured by Rutherford backscattering spectrometry (RBS) with 2 MeV-He ions using single-end accelerators of TIARA and Hiroshima University. Three different samples (labeled as "A", "B" and "C") were prepared for destructive analytical methods of X-TEM and XPS. Another sample, labeled as "D", was implanted with Ag ions to a lower fluence. X-TEM was conducted with JEM-2000EX operating at 200 KV for the sample A. Independently, cross-sectional scanning transmission electron microscopy (X-STEM) using JEM-3000F equipped with an energy dispersive X-ray spectrometer (EDS) was carried out to identify precipitates in the sample B. XPS using non-monochromatized Mg Kα radiation ($h\nu$ = 1253.6 eV) was performed with JEOL 9010.To obtain depth profile of Ag atoms in XPS of the sample C, it was etched with 0.8 keV-Ar ions at an etching rate of ~0.9 nm/s. XPS and sputtering were repeated until a Si $2p_{3/2}$ line form a Si substrate was obtained. XRD in θ- 2θ scan mode was carried out to address the issues related to crystal structure of precipitates in the samples.

2.3. Results and discussion

Fig. 2.1 shows backscattering (BS) spectra of four different samples of A, B and C, which were characterized by X-TEM, X-STEM and XPS, respectively. In all the BS spectra, the bimodal or multimodal distributions of Ag atoms are observed. Maximum Ag concentration occurs at about 110−120 nm, somewhat shallower than the projected range (R_p) of 350 keV-Ag^+ predicted by the SRIM calculation (155 nm) [9], assuming the density of SiO_2 to be 2.3 g/cm^3. This discrepancy could be explained by the fact that this simulation code does not take into account the dynamic evolution of the matrix. These spectra slightly differ in the width of the Ag peak located at 1.65 MeV and the yields at surface (1.52 MeV) and interface (1.73 MeV). The full widths at half maximum (FWHMs) of the Ag peak for the samples A, B and C become 27−32 keV, taking into account of a finite detector resolution (15 keV). The FWHMs of 27−32 keV correspond to the width of 50−60 nm, considerably smaller than the value of ~100 nm predicted by the SRIM [9]. Assuming that buried Ag zone forms in the SiO_2 layer [16] and the surface energy approximation [27] is valid, the zone thickness t can be roughly calculated by the following equation using the FWHM in a spectrum:

$$t = \frac{\mathrm{FWHM}}{N\{K\epsilon(E_0)+\epsilon(KE_0)/\cos\alpha\}},$$

where N is the atomic density of Ag (5.8×10^{22} atoms/cm^3), K the kinematic factor of ^{4}He-Ag (0.862), E_0 the incident energy of ^{4}He ions (2 MeV), $\epsilon(E_0)$ and $\epsilon(KE_0)$ the stopping cross

sections of Ag for ^{4}He ions with energies of E_0 and KE_0, respectively (95×10^{-15} eV cm^2 and 100×10^{-15} eV cm^2 [9]), α the outward-path angle of ^{4}He ions with respect to the sample normal (15°). The FWHMs (27−32 keV) yield the zone thicknesses of 25−30 nm through the aforementioned equation.

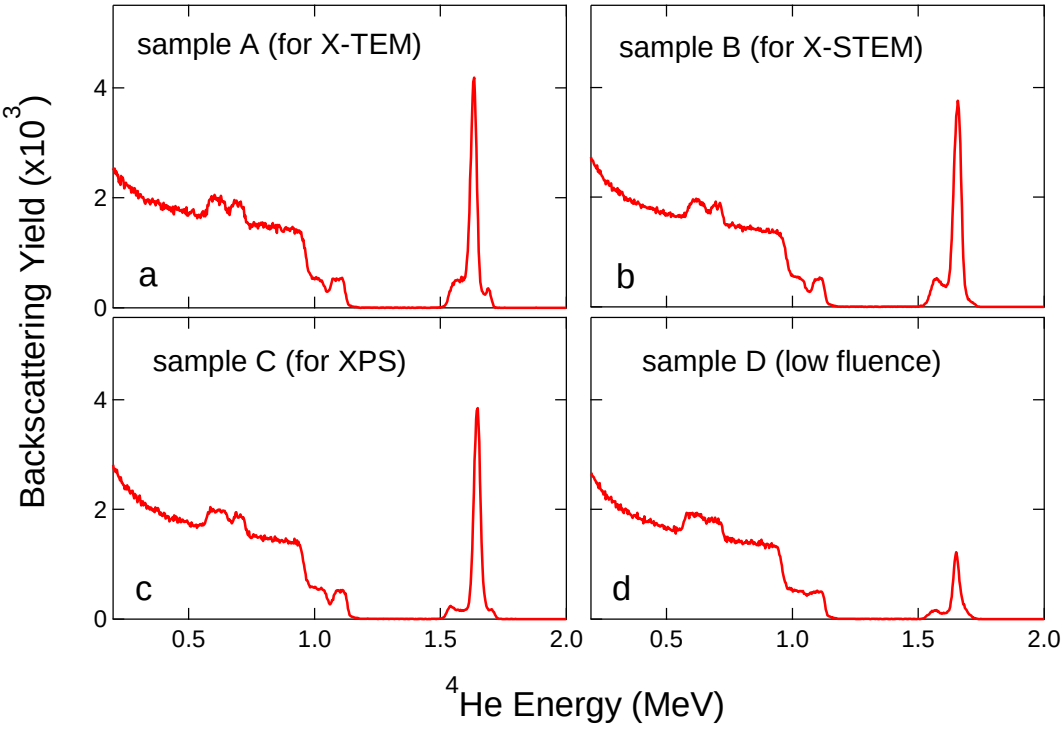

Fig. 2.1: RBS spectra of samples A (a), B (b), C (c) and D (d) implanted with 350 keV-Ag ions to fluences of 1.2, 1.2, 1.1 and 0.37×10^{17} ions/cm^2, respectively.

Judging from the RBS spectra, we suppose that the Ag depth distribution is very sensitive to the implantation parameters such as beam current density and implantation

temperature, which could not be controlled perfectly in this study. The amounts of Ag atoms calculated by the peak intensity are also a little bit different between the samples, and are estimated to be 1.2, 1.2 and 1.1×10^{17} ions/cm^2 for the samples A, B and C, respectively. In Fig. 2.1(d), the RBS spectrum of the sample implanted with Ag ions to a fluence of 0.37×10^{17} ions/cm^2. A sharp Ag peak similar to the peaks in Figs. 2.1(a)−(c) appears, indicative of a few tens thick buried Ag zone.

For better understanding of unusual profiles of Ag implanted into SiO_2/Si samples, thicker SiO_2 films (~ 700 nm) were implanted with 350 keV-Ag ions at two different beam-current densities, 0.6 and 4 μA/cm^2, and then analyzed by RBS. Fig. 2.2 shows BS spectra of the thicker SiO_2 films on Si implanted with 350 keV-Ag ions to a fluence of 1.2×10^{17} ions/cm^2 at the beam current densities of 0.6 μA/cm^2 (upper panel) and 4 μA/cm^2 (lower panel). As has been observed in Fig. 1, sharp Ag peaks indicate the presence of a few tens thick buried Ag zone. Surprisingly, the peak positions differ slightly, indicating that the depths of a buried Ag zone are not the same even though the implantation energies are identical. For the 4 μA/cm^2-implanted sample, the peak position of 1.64 MeV corresponds to the depth of 110 nm, while for the 0.6 μA/cm^2-implanted one, the peak position is 1.67 MeV, corresponding to the depth of 150 nm, assuming the density of SiO_2 to be 2.3 g/cm^3. The thickness of SiO_2 for the 4 μA/cm^2-implanted sample is found to be lower by about 40 nm than that for the 0.6

μA/cm^2-implanted sample. Therefore, the difference in the depth of a buried Ag zone between the two samples can be explained by the beam-current dependent erosion rate of SiO_2 surface. Another distinct feature in the two BS spectra is seen in the energy range of 1.2−1.6 MeV. A small bump located at 1.48 MeV, corresponding to a depth of 450 nm, can be clearly seen in the BS spectrum of the 4 μA/cm^2-implanted sample. This indicates that Ag atoms can migrate toward the depth much deeper than the projected range of 350 keV-Ag^+ at such a high beam current density. From the BS spectrum of the 4 μA/cm^2-implanted sample, the migrated Ag atoms are found to be located at a kind of trap site, e.g., defects or voids [28]. RBS analysis on the Ag implanted SiO_2/Si sample suggests that there are intrinsic defects or voids which can trap Ag atoms near the SiO_2/Si interface.

The sample A was subjected to characterization by X-TEM. Fig. 2 shows bright-field (BF) images for the sample A, which is implanted with 350 keV-Ag ions to a fluence of 1.2×10^{17} ions/cm^2. As can be seen in Fig. 3(a), an array of spherical Ag particles of 25−30 nm in diameter is located at a depth of ~125 nm. This situation is similar to the formation of buried Ag zone with thickness of 25−30 nm, in good agreement with the zone thickness estimated by RBS (25 nm). As described below, there are two distinct layers separated by the buried zone.

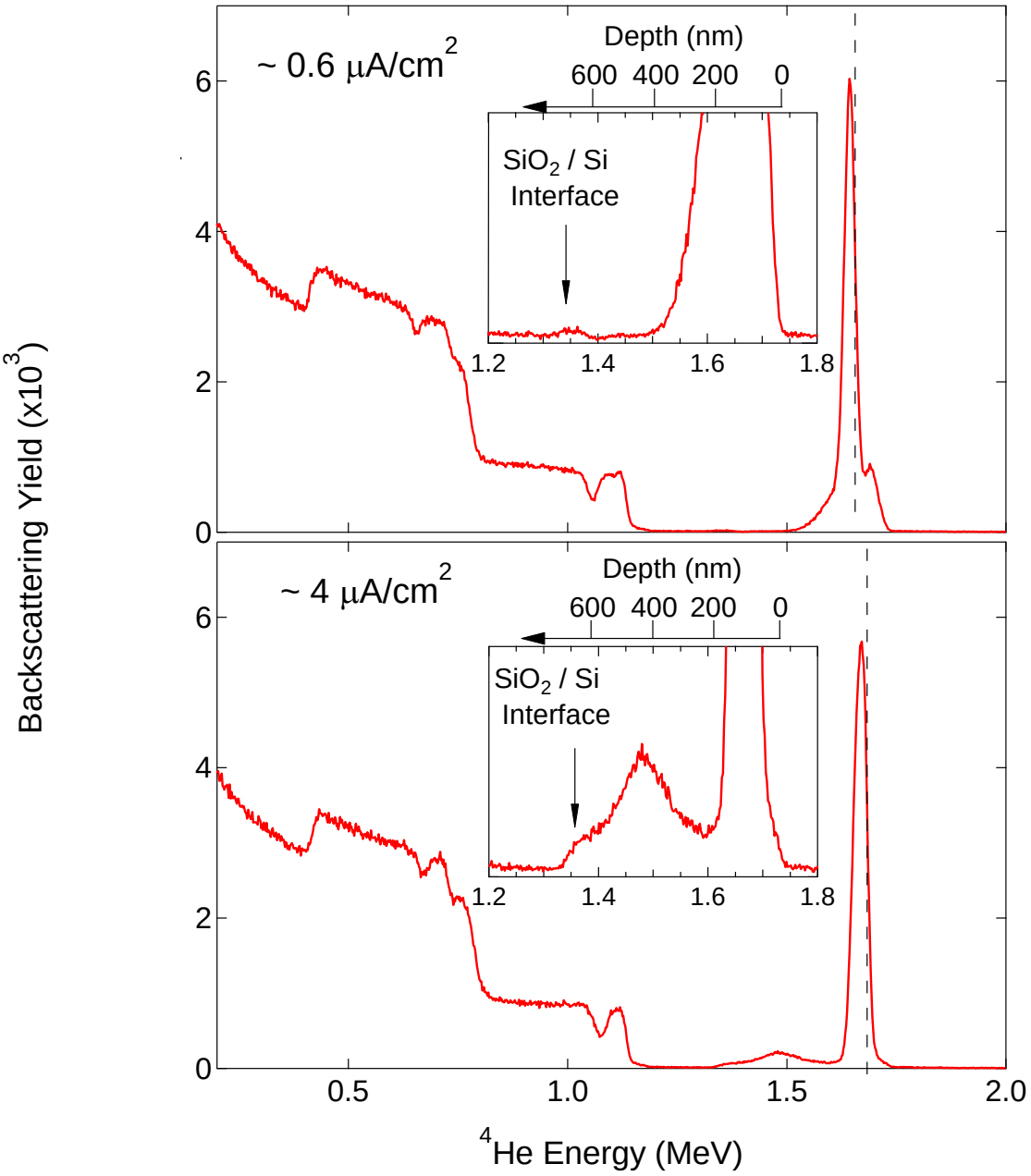

Fig. 2.2: RBS spectra of thicker SiO_2 films (~ 700 nm) on Si implanted with 350 keV-Ag ions to fluences of 1.2×10^{17} ions/cm^2 at beam current densities of 0.6 μA/cm^2 (upper panel) and 4 μA/cm^2 (lower panel). Ag peak position is indicated by a broken line in each spectrum. Insets are detailed spectra at energy range of 1.2−1.8 MeV along with depth scales in SiO_2. The SiO_2/Si interface is indicated by an arrow in each inset.

In the layer located at depths shallower than the buried zone, referred to as “surface zone” hereafter, Ag nanoparticles of 1−5 nm in diameter, depending on a distance from surface, are distributed. The particle size tends to increase as depth increases in the surface zone extending from 0 to 100 nm. It is well known that Ag is a fast diffuser which is easily trapped by defect produced by ion implantation [10,29]. According to the SRIM calculation [9], the number of vacancies (both of Si and O atoms) as well as implanted Ag atoms increases with depth up to 105 nm. Thus the depth-dependent size distribution is attributed to the vacancy and/or Ag atomic concentration profiles.

As shown in Figs. 2.3(a)−3(c), in the layer positioned at depths deeper than the buried zone, referred to as “interior zone” hereafter, nanoparticles of 2−3 nm in diameter are dispersed almost uniformly, and do not significantly change in their size as a function of depth, contrastive to the size distribution in the surface zone. The author concluded that these nanoparticles are made up of Ag atoms on the basis of the Ag depth profile shown in Fig. 2.1(a). In addition, some precipitates with size of 5−40 nm are present in the interior zone, as shown in Fig. 2.3(a). These precipitates might be formed at intrinsic defects or voids as shown in Fig. 2.2. Furthermore, tiny precipitates (< 2 nm in diameter) are clearly observed in the vicinity of the SiO_2/Si interface in Fig. 2.3(c). The tiny precipitates are found to be aligned along the interface. Such precipitates will be identified by STEM. Here we again emphasize the unexpected feature,

which is the coexistence of homogeneously dispersed Ag nanoparticles, some precipitates distributed irregularly and tiny precipitates aligned along the interface in the interior zone.

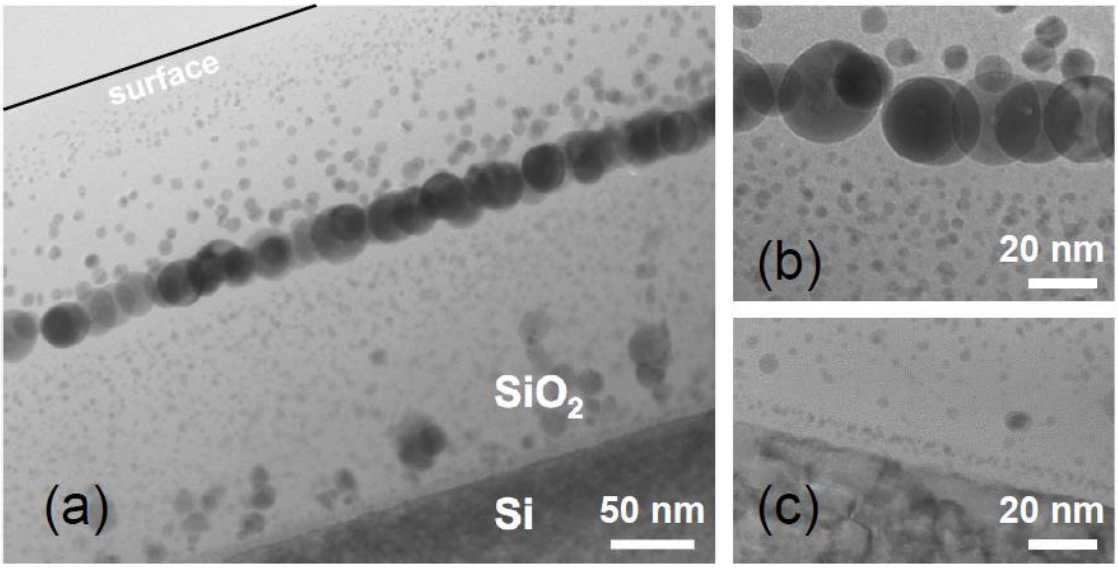

Fig. 2.3: Cross-sectional TEM bright-field images of the sample A. (a): a low magnification image, (b): a high magnification image of the buried zone, (c): a high magnification image at the SiO_2/Si interface.

Figs. 2.4(a) and (b) show magnified X-STEM BF and high-angle annular dark-field (HAADF) images, respectively, for the sample B. The two-dimensional (2D) array of Ag perfectly parallel to the surface can be seen in this micrograph. The Ag implanted SiO_2 is composed of three distinct zones -surface, buried and interior zones-, similar to that observed for the sample A. By the use of HAADF imaging, incoherent Z (atomic number)-contrast

STEM has been shown to provide direct compositionally sensitive structure images without the phase problem [30,31]. By comparing the images shown in Figs. 2.4(a) and (b), all the precipitates, including nanoparticles in the surface zone, spherical particle of 40 nm in diameter, irregularly distributed precipitates in the interior zone and small precipitates located along the SiO_2/Si interface, are found to be Ag nanoparticles. These are also identified as Ag precipitates by EDS line-analysis (not shown here).

It should be noted that the small precipitates that appear spatially distributed in the interior zone for the sample A (Fig. 2.3) are not visible in the sample B (Fig. 2.4). The explicit reason for this difference is not known at present, but a possible reason can be the difference in the concentration of intrinsic defects or voids between the two samples. Another reason might be linked to non-uniformity of the implantation process over the sample.

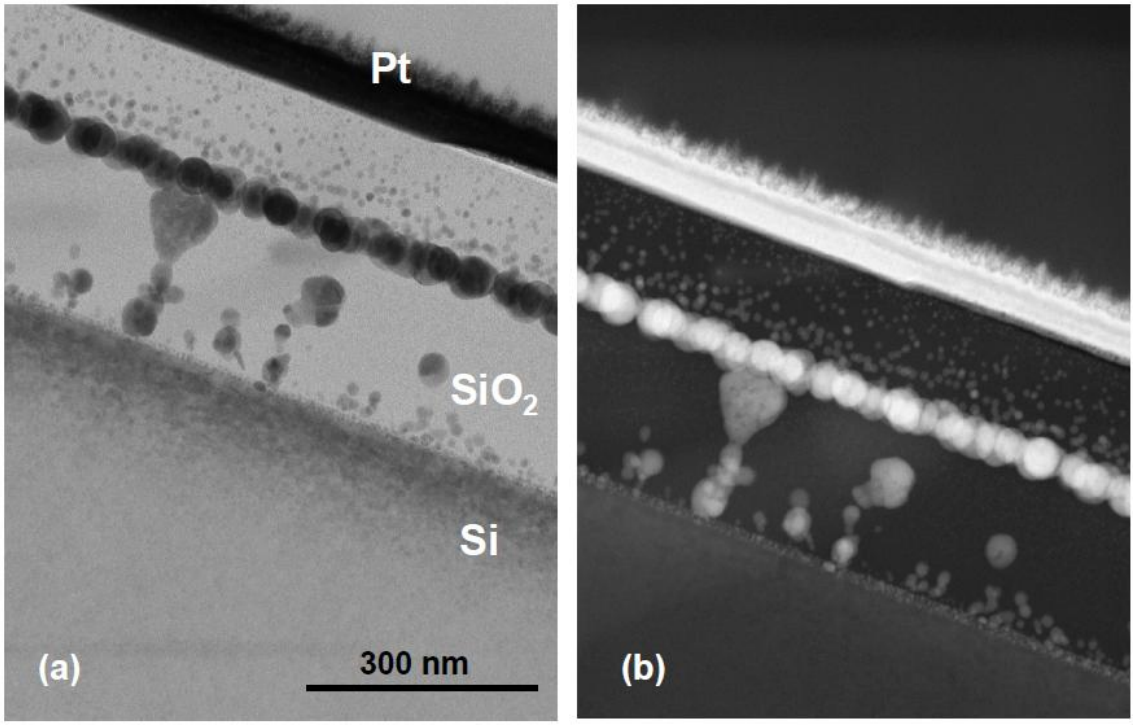

Fig. 2.4: A cross-sectional STEM bright field image (a) and a corresponding high-angle annular dark-field image (b) for the sample B.

The common features observed in the samples A and B are: (1) the distribution of Ag nanoparticles with depth-dependent size in the surface zone, which is already discussed above, (2) the formation of a 2D array of Ag nanoparticle, which has been observed and discussed in earlier works [11−13], (3) the existence of large Ag nanoparticles irregularly distributed in the interior zone, (4) the well-ordered arrangement of tiny Ag precipitates close to the SiO_2/Si interface. We shall discuss the features (3) and (4) below.

Considering the fact that the irregularly distributed precipitates are observed only in the interior zone, the formation of such nanoparticles is associated with the 2D array of Ag nanoparticles located on the way that Ag ions travel. The RBS spectrum of the sample implanted with 0.37×10^{17} ions/cm^2 in Fig. 2.1(d) shows the formation of nanoparticles at a depth of about 135 nm in, indicating that the 2D array of Ag nanoparticles forms at the early stage of implantation up to 10^{17} ions/cm^2. After the formation of Ag nanoparticles, they affect the trajectory of Ag ions. The Ag ions passing through an Ag nanoparticle come to rest at shallower depths, and would precipitate in the interior zone. Further, the interior zone includes intrinsic defects or voids near the SiO_2/Si interface. These defects or voids act as trap and nucleation sites for migrated Ag atoms.

The self-organized δ-layer of Ag nanoparticles at the SiO_2/Si interface is observed in the as-implanted samples for the first time. For the other system, Sb-implanted SiO_2/Si, Ignatova et al. [32] found such a δ-layer in as-implanted samples. Their implantation condition that the end of range of implanted ions is close to the depth of a SiO_2/Si interface is very similar to the present case. In fact, highly damaged Si layer is clearly seen in TEM micrographs (e.g. Fig. 2.3(a)). As pointed out by Heinig et al. [33], interface mixing at the interface might be responsible for the formation of small precipitations. A few nm thick layer of excess Si atoms in SiO_2 parallel to the interface can be formed as a result of the collisional mixing, and can act

as the nucleation sites for implanted ions. If the most probable effect is the interface mixing, the formation process of a δ-layer could be sensitive to the degree of interface mixing: the δ-layer is clearly seen in the sample A, but not so clear in the sample B. Another possible mechanism for the precipitation is due to compressive strain near the interface [34]. In these two mechanisms above, any thermal treatment after implantation is required for the formation of a δ-layer. Tsuji et al. [35] succeeded in the formation of Ag nanoparticles aligned along SiO_2/Si interface by implantation and subsequent annealing at 973 K. In this work, in contrast, tiny Ag precipitates are observed in the as-implanted samples. The author consider, therefore, that dynamic annealing during implantation with Ag ions play a role in self-organization of a δ-layer of Ag nanoparticles in the present case.

Next, the oxidation states of Ag precipitates in SiO_2 were explored with XPS and XRD. The measurements were performed 19−21 months later after implantation. In Fig. 2.5, the AP shifts from a bulk value (726.0 eV) along with Ag atomic concentrations deduced form line intensities are plotted as a function of sputtering time corresponding to depth in the sample C. The AP shifts are found to be zero around Ag concentration maximum, indicating that Ag precipitates are metallic. At surface and interior regions, the magnitudes of AP shifts are 0.2−0.5 eV, much smaller those for Ag_2O (1.7 eV), AgO (1.8 eV), and Ag_2S (1.2 eV) [25]. I conclude that such small shifts originate from neither oxidation nor sulfidation of Ag

nanoparticles, but from the size effect as has been observed for Au nanoparticles [36]. Thus Ag nanoparticles formed in SiO_2/Si matrices by ion implantation are found to be stable for 1.5 years at least. The XRD analysis also confirms this result. The XRD patterns in the range 2θ = 30−80° for the Ag-implanted samples stored in ambient conditions for 1.7 years (not shown here) exhibit only four diffracted lines, corresponding to (111), (200), (220) and (311) planes of a Ag crystal with an fcc structure.

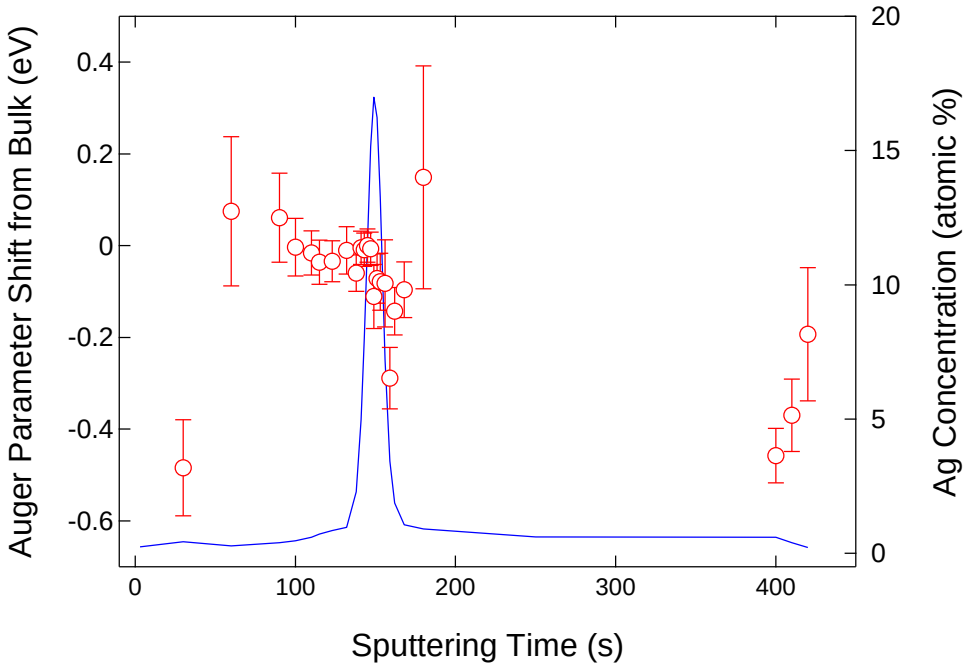

Fig. 2.5: XPS Auger parameter shifts from a bulk Ag (open circles) and Ag concentrations (solid line) as a function of sputtering time for the sample C. The Auger parameter of a bulk Ag is 726.0 eV, summing the Ag $3d_{5/2}$ binding energy (368.3 eV) and Ag $M_4N_{4,5}N_{4,5}$ Auger electron kinetic energy (357.7 eV) [25]. The negative shift value means that the Auger parameter is smaller than 726.0 eV.

Finally, the possible applications of Ag nanoparticles with well-ordered arrangements are briefly mentioned. The SiO_2 substrates including such Ag nanoparticles can be used as *plasmonic sensing* and stable SERS substrates [2,3] after removing SiO_2 top layers. Tiny Ag nanoparticles aligned along the SiO_2/Si interface are expected to exhibit Coulomb Blockade [17] when SiO_2 top layers including irregularly arranged larger Ag nanoparticles are removed appropriately.

2.4. Conclusion

The SiO_2/Si substrates were implanted with 350 keV-Ag ions to fluences of $0.37-1.2\times10^{17}$ ions/cm^2, and characterized by means of RBS, X-TEM, X-STEM, XPS and XRD. Three distinct zones are observed in the high fluence Ag-implanted samples. The surface zone includes Ag nanoparticles with size of 1−5 nm, depending on a distance from surface. The 2D array of Ag nanoparticles of 25−40 nm in diameter forms at a depth of ~130 nm, named as buried zone. In the interior zone, the δ-layer of tiny Ag nanoparticles is aligned along the SiO_2/Si interface, together with randomly distributed Ag nanoparticles with various sizes (5−40 nm). The Ag nanoparticles embedded in the SiO_2/Si is found to be stable against oxidation and sulfidation when stored in ambient conditions for more than one and a half year.

References

[1] V. M. Shalaev, *Optical Properties of Nanostructured Random Media*, (Springer Verlag, Berlin, 2002).

[2] X. Zhang, J. Zhao, A. V. Whitnu, J. W. Elam & R. P. Van Duyne, J. Am. Chem. Soc, 2006, **128**, 10304.

[3] F. H. Scholes, A. Bendavid, F. L. Glenn, M. Critchley, T. J. Davis and B. A. Sexton, J. Raman Spectrosc. 2008, **39**, 673.

[4] S. Charvet, R. Madelon, F. Gourilleau & R. Rizk, J. Appl. Phys. 1999, **85**, 4032.

[5] H. Mertens, J. Verhoeven, A. Polman & F. D. Tichelaar, Appl. Phys. Lett. 2004, **85**, 1317.

[6] G. De, L. Tapfer, M. Catalano, G. Battaglin, F. Caccavale, F. Gonella, P. Mazzoldi & R. F. Haglund, Jr., Appl. Phys. Lett. 1996, **68**, 3820.

[7] P. Mazzoldi and G. Mattei, Phys. Stat. Sol. A 2007, **204**, 621.

[8] A. L. Stepanov and V. N. Popok, J. Appl. Spectrosc. 2001, **68**, 164.

[9] J. F. Ziegler, J. P. Biersack & U. Littmark, *The Stopping and Ranages of Ions in Solids* (Pergamon, NewYork, 1985), and available at the web site: http:// www.srim.org

[10] G. W. Arnold & J. A. Borders, J. Appl. Phys. 1997, **48**, 1488.

[11] N. Matsunami & H. Hosono, Appl. Phys. Lett. 1993, **63**, 2050.

[12] Z. Liu, H. Li, X. Feng, S. Ren, Z. Liu & B. Lu, J. Appl. Phys. 1998, **84**, 1913.

[13] Z.Liu, H. Wang, H. Li & X. Wang, Appl. Phys. Lett. 1998, **71**, 1823.

[14] N. Arai, H. Tsuji, N. Gotoh, T. Minotani, T. Ishibashi, K. Adachi, H. Kotaki, Y. Gotoh & J. Ishikawa, J. Phys: Conf. Ser. 2007, **61**, 41.

[15] J. R. Bird & J. S. Williams, *Ion Beams for Materials Analysis* (Academic Press, Australia, 1989).

[16] R. Carles, C. Farcau, C. Bonafos, G. Benassayag, B. Pécassou & A. Zwick, Nanotechnology 2009, **20**, 355305.

[17] H. Tsuji, N. Arai, T. Matsumoto, K. Ueno, Y. Gotoh, K. Adachi, H. Kotaki & J. Ishikawa, Appl. Surf. Sci. 2004, **238**, 132.

[18] W. Cai, H. Zhog & L. Zhang, J. Appl. Phys. 1998, **83**, 1705.

[19] M. Hillenkamp, G. Di Domenicantonio & O. Eugster, Nanotechnology 2007, **18**, 015702.

[20] P. Benzo, L. Cattano, C. Farcau. A. Andreozzi, M. Perego, G. Benassayag, B. Pécassou, R. Carles & C. Bonafos, J. Appl. Phys. 2011, **109**, 103524.

[21] J. L. Elechiguerra, L. L.-Lopez, C. Liu, D. G.-Gutierrez, A. C.-Bragado & M. J. Yacaman, Chem. Mater. 2005, **17**, 6042.

[22] M. D. Mcmahon, R. Lopez, H. M. Meyer III, L. C. Feldman & R. F. Haglund Jr., Appl. Phys. B 2005, **80**, 915.

[23] W. Cao & H. E. E.-Ali, Mater. Lett. 2009, **63**, 2263.

[24] C.D. Wagner, Faraday Discuss. Chem. Soc. 1975, **60**, 291.

[25] C. D. Wagner, D.E. Passoja, H. F. Hillery, T. G. Kinisky, H. A. Six, W. T. Jansen, J. A. Taylor, J. Vac. Sci. Technol. 1982, **21**, 933.

[26] V. K. Kaushik, J. Electr. Spectrosc. Relat. Phenom. 1991, **56**, 273.

[27] W. K. Chu, J.W. Mayer & M. A. Nicolet, *Backscattering Spectrometry* (San Diego, CA, 1978).

[28] G. W. Rubloff, J. Vac Sci. Technol. 1990; A8:1857-63.

[29] R. Espiau de Lamaestre, H. Béa, H. Bernas, J. Belloni & J. L. Marignier, Phys. Rev. B 2007, **76**, 205431.

[30] P. M. Voyles, D. A. Muller, J. L. Grazul, P. H. Citrin & H.-J. L. Gossmann, Nature 2002, **416**, 826.

[31] A. R. Lupini & S. J. Pennycook, Ultramicroscopy 2003, **96**, 313.

[32] V. A. Ignatova, O. I. Lebedev, U. Wätjen, L. Van Vaeck, J. Van Landuyt, R. Gijbels & F. Adams, J. Appl. Phys. 2002, **92**, 4336.

[33] K. H. Heinig, T. Müller, B. Schmidt, M. Strobel & W. Möller, Appl. Phys. A 2003, **77**, 17.

[34] A. Nakajima, H. Nakao, H. Ueno, T. Futatsugi, & N. Yokoyama, J. Vac. Sci. Technol. B 1999, **17**, 1317.

[35] H. Tsuji, N. Arai, T. Matsumoto, K. Ueno, K. Adachi, H. Kotaki, Y. Gotoh, J. Ishikawa, Surf. Coat. Technol. 2005, **196**, 39.

[36] S. Zafeiratos & S. Kennou, Surf. Sci. 1999, **443**, 238.

Chapter 3

Modification of Ag and Au nanoparticles by using plasma and ion beams

3.1. Introduction

Metal nanoparticles exhibit novel physico-chemical properties, quite different from those of bulk materials, and have potential applications in a wide variety of scientific fields including catalysis [1,2], electronics [3,4], plasmonics [5,6], biotechnology [7]. In particular, extensive studies have performed for silver nanoparticles (NPs) because of an attractive optical property, which is a strong extinction band in the visible range. The strong optical extinction arises from the surface plasmon oscillation of conduction electrons coupled to an external electromagnetic field. The surface plasmon resonance of silver NPs is being used for the development of chemical and biological sensors [8−11]. In addition, the plasmon oscillation due to incident light sometimes results in surface enhanced Raman scattering (SERS), which is expected to be a technique for single molecule detection [12−14]. The control of the surface plasmon resonance property, which is well characterized by the plasmon resonance wavelength λ_p and line width $\Delta\omega_p$, is required for silver NPs supported on substrates to realize such applications.

In the survey of the λ_p of supported silver NPs [15−21], it is found that the reported λ_p values are between 380 and 500 nm, larger than that predicted by the Mie's theory (370 nm [22]); the experimental data differs lab by lab. Further, all the optical extinction spectra

reported are found to be much broader than the calculated one [22], with a few exceptions [19,20]. The shape and density (or degree of dispersion) of silver NPs on substrates are, of course, factors to govern their optical properties, but the variation of the reported λ_p as well as the discrepancy between experimental and theoretical extinction spectra cannot be explained completely by these two factors. To control the surface plasmon properties, all the occurring effects should be clarified. The author found that the shortest wavelengths and narrowest spectra were simultaneously obtained for the following cases; 1) as shown in Ref. 19, silver NPs were deposited in vacuum and then in situ optical extinction spectra were taken, and 2) as has been found in Ref. 20, silver NPs were post-annealed at temperatures above 473 K. Moreover, experimental extinction spectra of silver NPs embedded in a matrix are close to the calculated one [23]. These facts suggest that the origin of large differences between the experimental and theoretical extinction spectra of supported silver NPs can be unavoidable impurity adsorption during and/or after sample preparations. The adsorption of impurities on the silver NPs is known to increase refractive index of their surroundings, leading to the redshift of resonance wavelength and the broader spectrum compared to those of bare NPs [8,9,11,19,24], referred to as chemical interface damping [19]. In this article, the author demonstrates that surface cleaning of silver NPs by a plasma treatment results in the surface

plasmon characteristics similar to the prediction by Mie's theory. The present work reveals the intrinsic optical properties of silver NPs deposited on substrates.

In addition to the motivation described above, an intense and sharp LSPR peak of purified Ag NPs is required for T-LSPR sensors as has been mentioned in the section 1.2 of Chapter 1. Such a desired LSPR characteristic would be obtained by energetic ion processes including a plasma treatment and ion irradiation.

Further, gold nanoparticles (Au NPs) exhibit strong optical extinction due to localized surface plasmon resonance (LSPR) in the visible range. The Au NPs on transparent dielectrics are being applied to chemical and biological sensors in which changes in the LSPR features, including resonance wavelength, width and intensity, are detected with the presence of analytes. To maintain a high performance of such sensors, purification of Au NP surfaces is needed. In the present work, plasma and ion sputtering have been employed to purify the Au NP surfaces on the basis of my study for Ag NPs.

3.2. Experimental methods

The substrate used was commercially available synthetic silica SiO_2, which was cleaned with ethanol and dried in an ambient air prior to preparing NPs. Ag and Au NPs were

deposited on SiO_2 by an rf magnetron sputtering method. The base pressure of the apparatus was lower than 1.3×10^{-5} Pa. The pressure of Ar gas was 0.14 Pa and substrate temperature was kept at 473 K during the sputter deposition for 2 min. The deposition rate was estimated to be 0.5−1 nm min^{-1}. Plasma treatment with Ar was performed by using Harrick Plasma PDC-32G operated at a power of 18 W. In the present work, an inert Ar gas was used to avoid chemical reactions, e.g. oxidation, occurred at silver NP surfaces. The pressure of Ar gas was 20 Pa during plasma exposure. N ions with an energy of 350 keV, produced from the 400 kV ion implanter of at Takasaki Ion Accelerator for Radiation Application (TIARA), were used to irradiate Ag NPs. Before and after plasma and ion treatments, UV-vis extinction measurements were immediately carried out in standard transmission geometry with unpolarized light in the wavelength range of 200−800 nm. Raman scattering spectroscopy with a backscattering geometry was conducted with an Ar ion laser (λ = 514.5 nm). The author expects an extremely high sensitivity for adsorbed molecules on silver NPs due to SERS in the present analysis. Heavily doped silicon wafers ($\rho = 10^{-2}$–10^{-3} Ω cm) without removing a native oxide layer were also used as a substrate for silver NPs prepared under the conditions same as the above. The Ag/Si samples were exposed to plasma and then characterized by means of a field emission scanning electron microscope (SEM) operating at 15 kV and Rutherford

backscattering spectrometry (RBS) with 2.3 MeV-He ions. As will be shown later (in Fig. 3.6 a), silver NPs with 10−20 nm in diameter were dispersed on the Si substrate, along with a minor component of larger particles of 30−50 nm.

In the case of modification of Au NPs, Ar ion beams with an energy of 0.4 keV were used in XPS preparation chamber. X-ray photoelectron spectroscopy (XPS) using Mg Kα radiation ($h\nu$ = 1253.6 eV) was performed with a JPS-9010 X-ray photoelectron spectrometer (JEOL, Japan). The sample was placed in the XPS equipment and irradiated with Ar ions at an energy of 0.4 keV at a current density of ~50 μA cm^{-2}, corresponding to an ion flux of 3.4×10^{14} ions cm^{-2} s^{-1}. A pulsed ion beam, whose duty rate could be varied from 10% to 100%, was used to irradiate the sample for less than 1 s. In XPS, the peak energies were calibrated by locating the C1s peak, which occurs at 285.0 eV. Ar Plasma exposure was conducted with PDC-32G under the same conditions above.

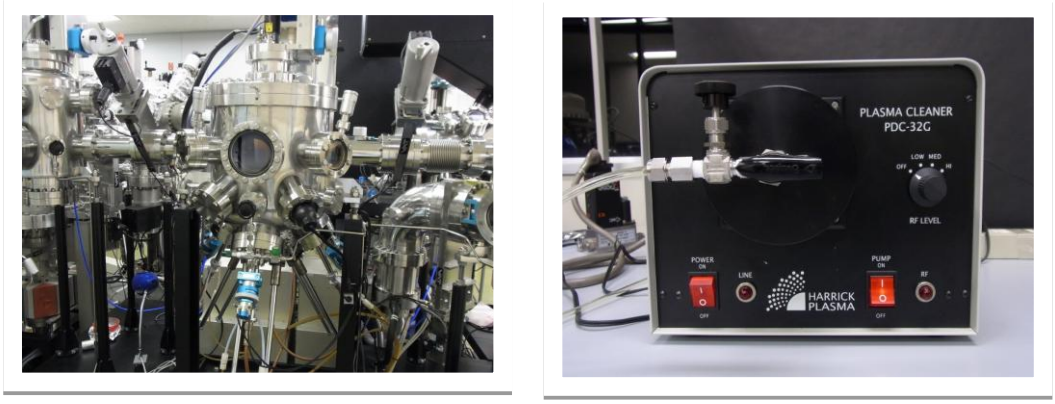

Fig. 3.1: Photographs of apparatus for Ag and Au NP preparation (left) and plasma exposure (right).

3. 3. Results and discussion

3.3.1. Modification of Ag nanoparticles with Ar plasma

Fig. 3.2 shows a series of optical extinction spectra of Ag/SiO_2 samples before and after plasma treatments. The plasmon resonance wavelength λ_p changes from 465 nm for the untreated sample to 415 nm for the sample exposed to Ar plasma for 300 s. The line width of a plasmon resonance band located at 300−600 nm decreases with increasing exposure time as well. Remarkable blue-shift and sharpening of the plasmon resonance can be seen. Thus the extinction spectra of plasma treated samples approach the spectrum calculated by Mie's theory [22]. In addition to such changes, a bump at ~350 nm, assigned to out-of-plane quadrupole plasmon resonance [25], emerges in the extinction spectrum of Ag/SiO_2 exposed to plasma.

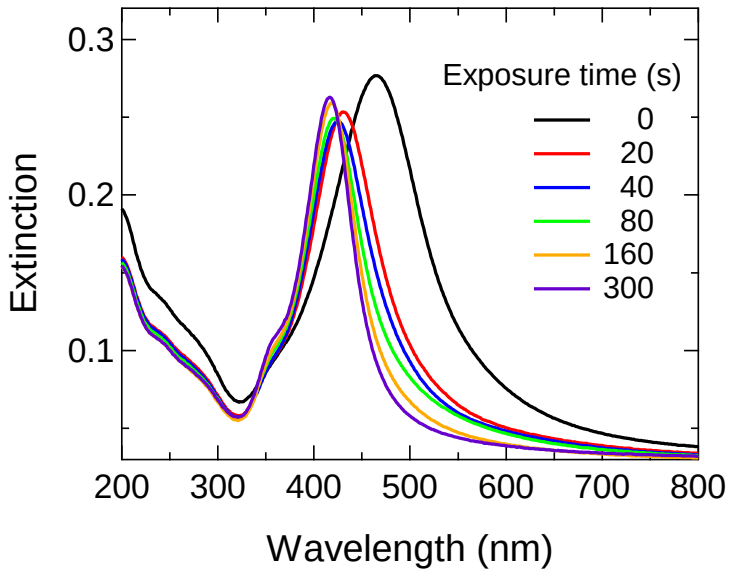

Fig. 3.2: Optical absorption spectra of Ag/SiO_2 before and after plasma treatment for 20, 40, 80, 160 and 300 s.

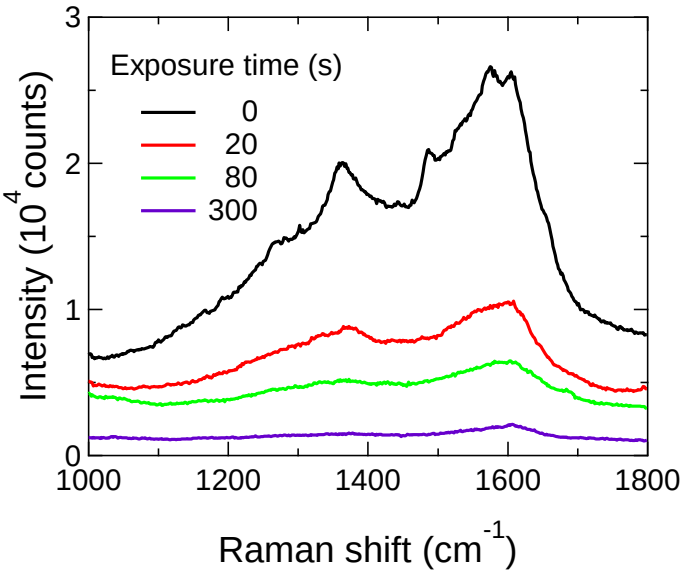

Fig. 3.3: Raman spectra of Ag/SiO_2 before and after plasma treatments for 20, 80 and 300 s.

On the assumption that impurity adsorption blinds intrinsic optical properties of silver NPs on substrates, molecules adsorbed on them were identified by Raman scattering. Fig. 3.3 shows Raman spectra of the samples before and after plasma treatments. The spectrum of the sample without plasma exposure has two prominent lines at 1350 and 1600 cm^{-1}, assigned to the disorder induced line (*D* band) [26] and E_{2g} line (*G* band) [26], respectively, of graphitic materials, which is similar to the SERS spectrum of hydrogenated amorphous carbon clusters deposited on electrochemically-roughened silver [27]. Impurities such as hydrogenated amorphous carbon can be clearly detected on the as-prepared sample. The Raman spectra abruptly decrease in intensity with increasing plasma exposure time, and are eventually almost invisible, indicating that the plasma effectively removes impurities on the samples. As can be

seen in Fig. 3.4, the Raman peak intensity is correlated well with the peak position λ_p, which is a clear indication that hydrocarbons are adsorbed on the as-prepared silver NP surfaces and are removed by plasma exposure.

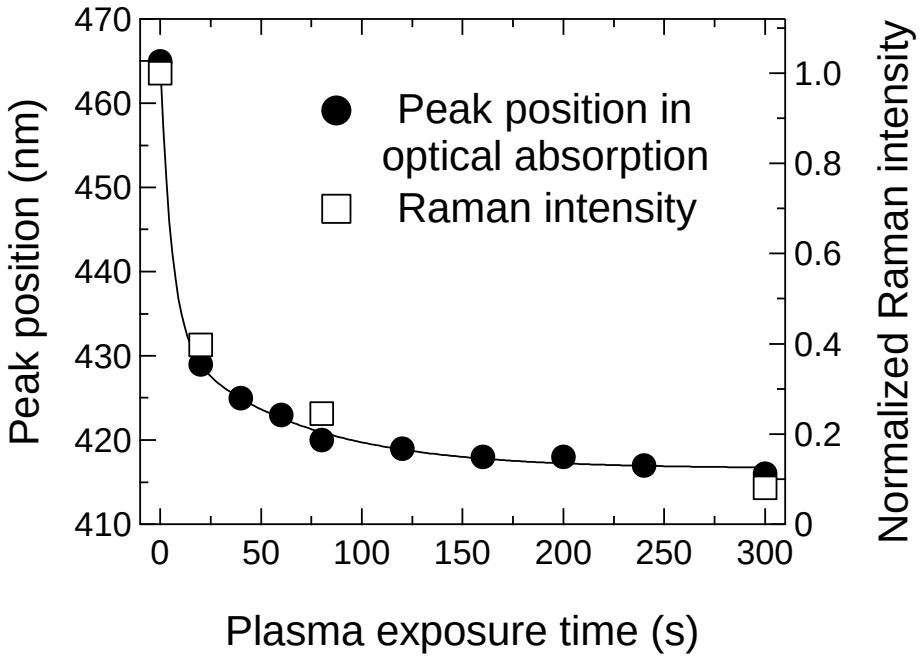

Fig. 3.4: Peak positions of surface plasmon resonance band in optical absorption spectra (filled circles) and normalized Raman intensities (open squares) as a function of plasma exposure time. A line is drawn to guide the eyes.

So far the changes in plasmon resonance characteristics of silver NPs have been discussed in terms of impurity elimination by plasma treatments. In addition, the characteristics would be also affected by surface morphology of silver NPs. Next, morphological changes of the sample exposed to plasma are examined. Atomic force microscopy (AFM) may provide information about surface morphology of silver NPs. The author tried to observe the Ag NPs with AFM, but the images depend strongly on a cantilever used. Therefore, I switched the observation method to scanning electron microscopy (SEM). To avoid surface charging during SEM observation, I used heavily doped single crystalline Si with a native oxide layer, instead of insulating SiO_2 substrates. Figure 3.5 presents scanning electron micrographs of the samples before and after plasma exposure up to 300 s. Except for occasional coalescence of larger particles, the size and shape are almost unchanged both for the smaller and larger NPs even after prolonged plasma exposure. Extremely mild treatments by plasma at room temperature allow us to clean the surfaces with maintaining their morphology. The variation of the number of silver atoms after plasma exposure is a key issue to examine how plasma works on silver NPs. It has been found that silver atoms are hard to be sputtered away by plasma exposure, as seen in Fig. 3.6 depicting total amounts of silver atoms estimated by RBS as a function of plasma exposure time. Judging from SEM and RBS data, the adhered impurities were only

removed from the silver surfaces by plasma. Thus the changes in optical extinction spectra of silver NPs exposed to plasma are resulted not from morphological alterations but from the removal of hydrocarbons.

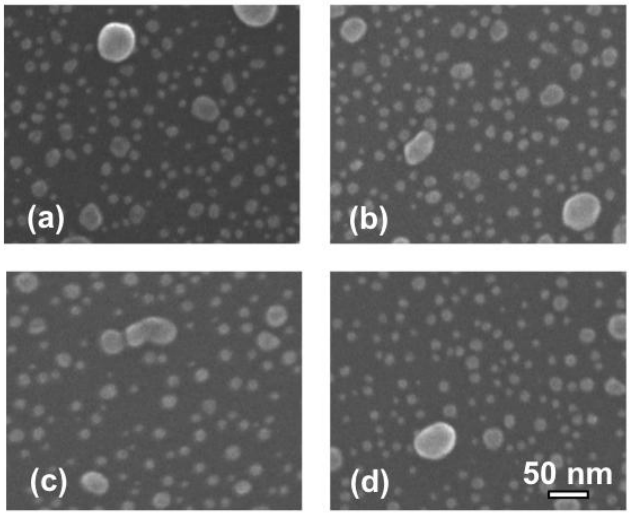

Fig. 3.5: SEM images of Ag/Si samples before (a) and after plasma treatments for 20 s (b), 80 s (c) and 300 s (d).

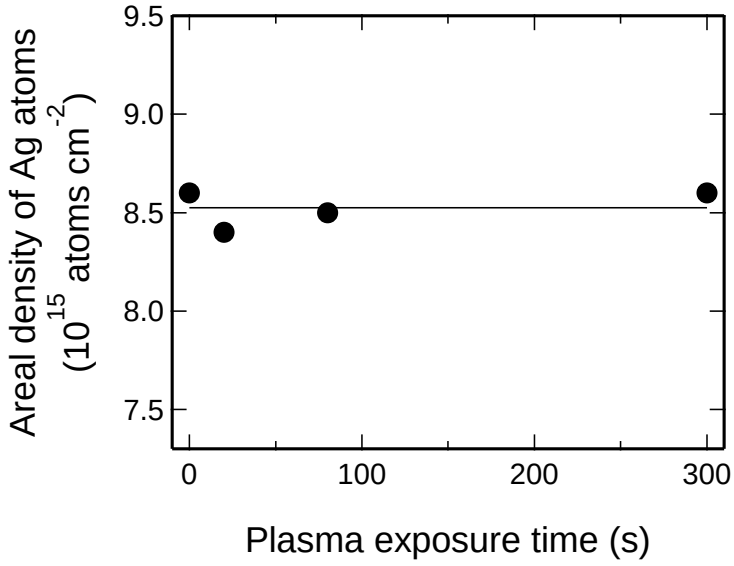

Fig. 3.6: Areal densities of silver atoms estimated by RBS as a function of plasma exposure time. A line is drawn to guide the eyes.

3.3.2. Modification of Ag nanoparticles by N ion irradiation

In the previous section, a sharp LSPR band can be realized by detaching hydrocarbon. Ion irradiation would be expected to bring about a similar effect caused by sputtering as well as an electronic excitation. Fig. 3.7 shows a series of optical extinction spectra of Ag/SiO_2 samples irradiated with 350 keV-N ions. Surprisingly, the extinction for the sample irradiated with 1.0×10^{12} N^+/cm^2 becomes higher than that for un-irradiated sample. In addition, the peak position is shifted toward longer wavelength. The enhancement and red-shift of an LSPR band can be explained by the inverse process of plasma cleaning as seen in the previous section. That is to say, irradiation with N ions causes attachment of impurities. I often found hydrocarbon adsorption onto sample surface during RBS analysis with MeV He ions. If hydrocarbon adsorption is a dominant effect on the change in LSPR band, the Raman spectrum of hydrocarbon increases in intensity. However, the intensity of Raman spectra decreases with the increase in fluence as can be seen in Fig. 3.8. Thus, the effect other than hydrocarbon adsorption should be considered to explain the observed enhancement and red-shift of the LSPR band.

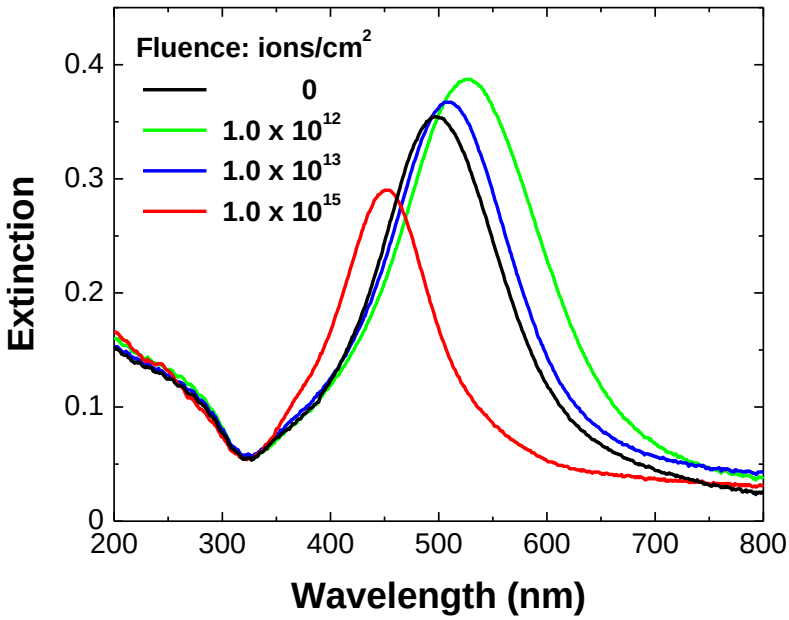

Fig. 3.7: Optical extinction spectra of Ag/SiO_2 irradiated with 350 keV N ions. Irradiation fluences are 0, 1.0×10^{12}, 1.0×10^{13}, 1.0×10^{15} N^+/cm^2.

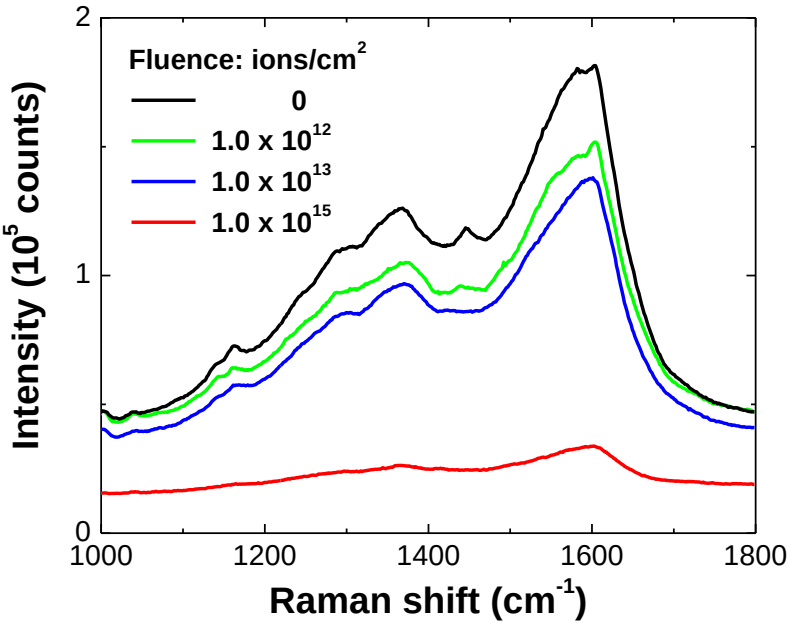

Fig. 3.8: Raman spectra of Ag/SiO_2 irradiated with 350 keV N ions. Irradiation fluences are 0, 1.0×10^{12}, 1.0×10^{13}, 1.0×10^{15} N^+/cm^2.

The enhancement and red-shift can be originated from *irradiation-induced crystallization* of Ag clusters. The crystallization would enhance the number of free electrons which participate in the plasmon oscillation and reduce inter-particle distances due to enhancement in an Ag NP size, resulting the enhancement and redshift of an LSPR band. At a fluence of 1.0×10^{13} N^+/cm^2, both the extinction and Raman intensities are lower than those at a fluence of 1.0×10^{12} N^+/cm^2, indicating that hydrocarbon desorption dominates. Upon further irradiation (1.0×10^{15} N^+/cm^2), sputtering by N ion reduces the number of Ag atoms, i.e., electrons participating in the plasmon oscillation, and the inter-particle distance becomes larger, leading to weakening, sharpening and blue-shift of LSPR peak.

3.3.3. Modification of Au nanoparticles by Ar plasma exposure and Ar ion irradiation

Fig. 3.9 shows a series of optical extinction spectra of Au/SiO_2 samples before and after plasma treatments. In Fig. 3.10 the LSPR positions are plotted as a function of plasma exposure time. The plasmon resonance wavelength λ_p changes from 614 nm for the untreated sample to 576 nm for the sample exposed to Ar plasma for 300 s. The line width of a plasmon resonance band located at 500−700 nm decreases with increasing exposure time as well. Remarkable blue-shift and sharpening of the plasmon resonance can be seen. In contrast to the

case for Ag NP, the intensity of LSPR for Au remarkably decreases (from 0.31 to 0.21 in an optical density) with increasing plasma exposure time.

Fig. 3.11 depicts particle size distributions indicated by histograms before and after plasma exposure for 300 s. SEM pictures are inserted in each graph. A large difference in the distribution at sizes less than 10 nm between un-exposed and exposed Au NPs can be recognized. Au NPs with tiny size (< 10 nm) are found to be diminished. Rutherford backscattering spectrometry reveals that the Au content decreases from 1.8×10^{16} to 1.6×10^{16} Au atoms/cm^2 after Ar plasma exposure. The remarkable reduction in the LSPR intensity observed in the Au NP array exposed to Ar plasma cannot be explained by the removal of such tiny Au NPs. Clearly coalescence of Au NPs is observed in the micrograph of the sample exposed to Ar plasma. The coalescence results in the increase in a distance between Au NPs. Further, impurities adsorbed on Au NP surfaces may be released by Ar plasma exposure as has been observed in the Ag NP aggregate. The evidence of such release can be obtained by Raman scattering spectroscopy, but the signal intensity for impurities was too low to observe the change in the amount of impurities before and after Ar plasma exposure because the SERS effect is not enough in the case of Au NPs with Ar ion laser (λ = 514.5 nm). The relationship between carbon elimination and LSPR characteristic of Au NP array can be seen below.

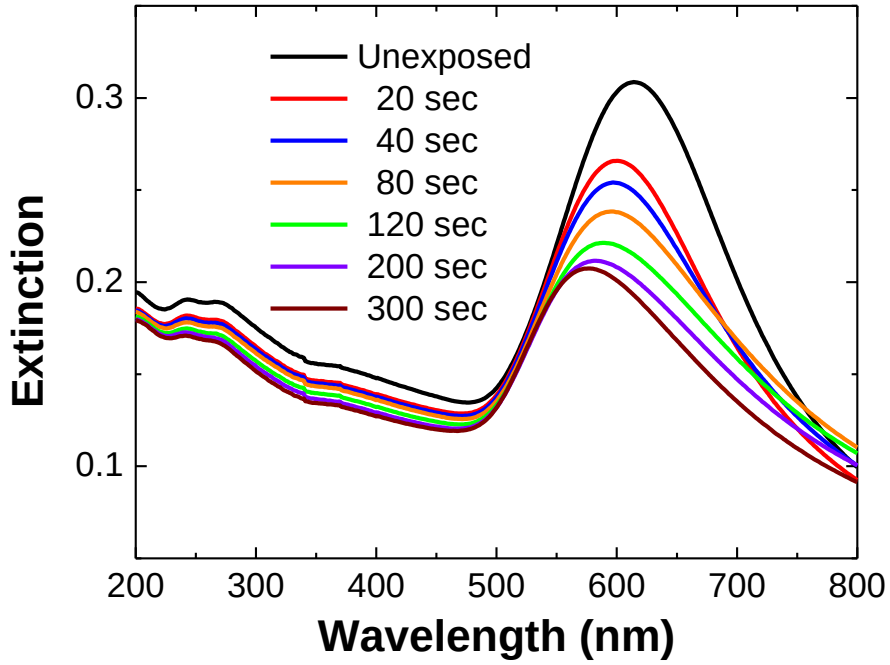

Fig. 3.9: Optical extinction spectra of Au/SiO_2 before and after plasma treatment for 20, 40, 80, 120, 200 and 300 s.

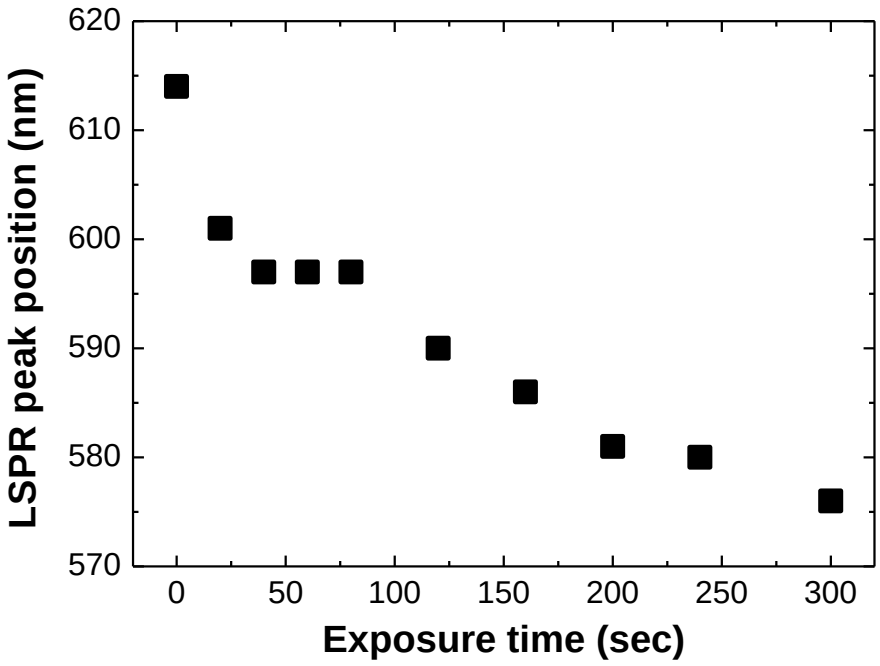

Fig. 3.10: The LSPR peak positions as a function of plasma exposure time.

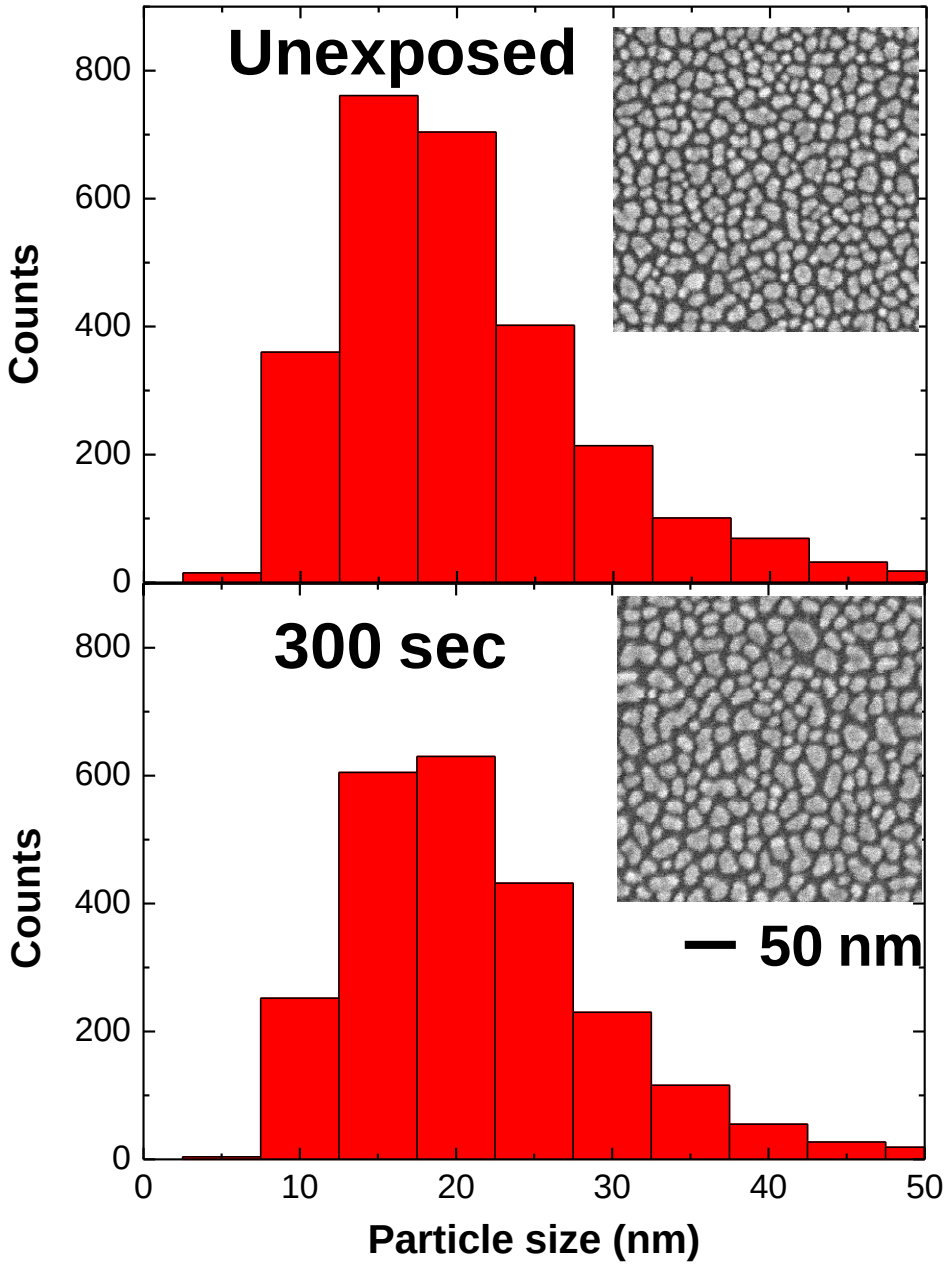

Fig. 3.11: Size distributions of Au NPs before (top) and after Ar plasma exposure. Inserts are SEM micrographs.

Fig. 3.12 shows a series of optical extinction spectra of Au/SiO_2 samples before and after Ar ion irradiation for 0.5, 1, 2 s. The tendency is the same as the case of plasma exposure. In Fig. 3.13, the LSPR positions are plotted as a function of irradiation time. Again the remarkable reduction in the LSPR intensity is clearly observed in Ar-irradiated Au NP array. Fig. 3.14 shows particle size distributions indicated by histograms before and after 0.4 keV-Ar ion irradiation for 2 s. The size distributions are almost unchanged except at size of 10 nm. SEM photographs are inserted in each graph. As mentioned in the section of experimental methods, 0.4 keV-Ar ion irradiation was conducted in XPS chamber. The XPS analysis can provide information on cleanness of Au NPs. As shown in Fig. 3.15, the intensity ratio of C 1*s* to Au $4f_{7/2}$ photoelectrons decreases from 0.065 to 0.012 as irradiation time increases. As described in ref [28], a metal sphere coated with a dielectric exhibits an increase in extinction cross-section and wavelength of the resonance peak, as the thickness of the dielectric layer grows. Conversely, the removal of C contaminants causes a reduction in SPR intensity, along with a shift in the resonance position toward shorter wavelength, as has been shown experimentally [29]. Thus, the remarkable reduction in LSPR intensity observed in Au NP arrays exposed to Ar plasma and irradiated with Ar ions is resulted from desorption of carbon impurities as well as the reduction of an inter-particle distance.

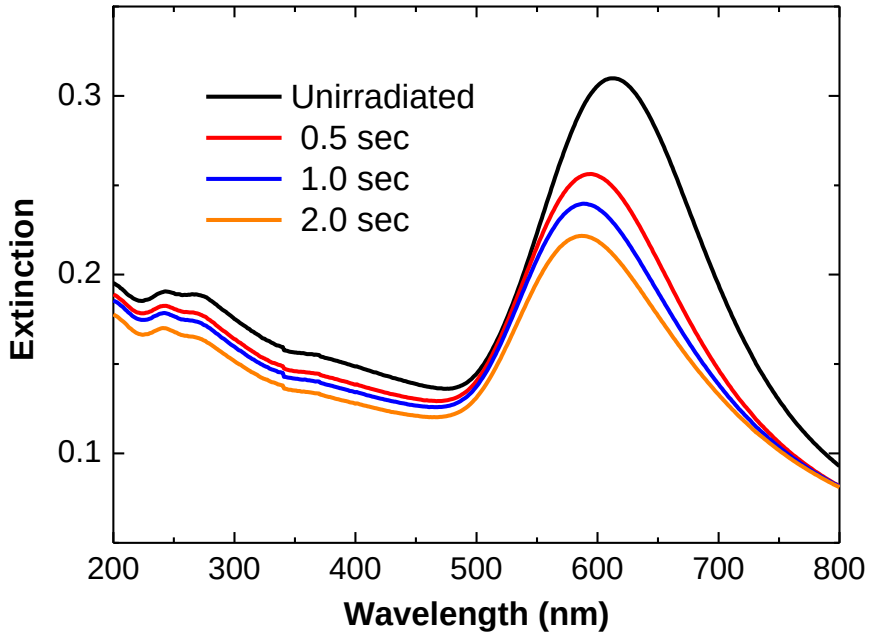

Fig. 3.12: Optical extinction spectra of Au/SiO_2 before and after 0.4 keV-Ar irradiation for 0.5, 1, 2 s.

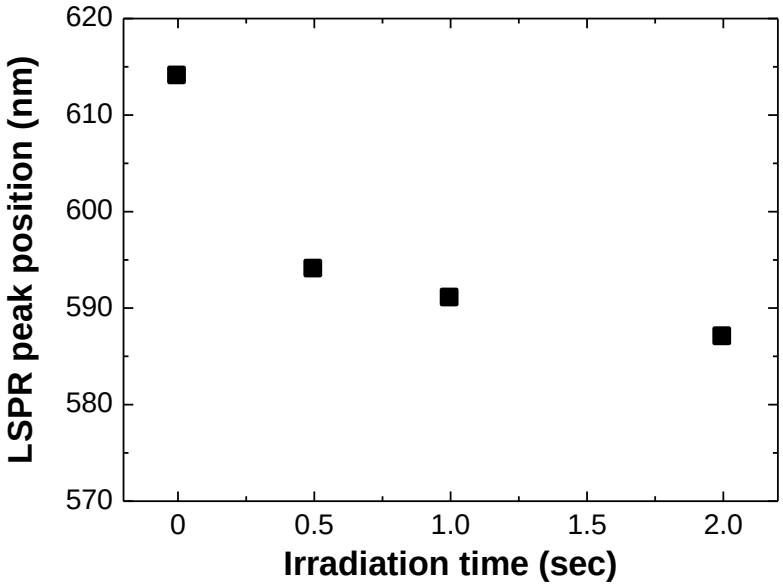

Fig. 3.13: The LSPR peak positions as a function of irradiation time.

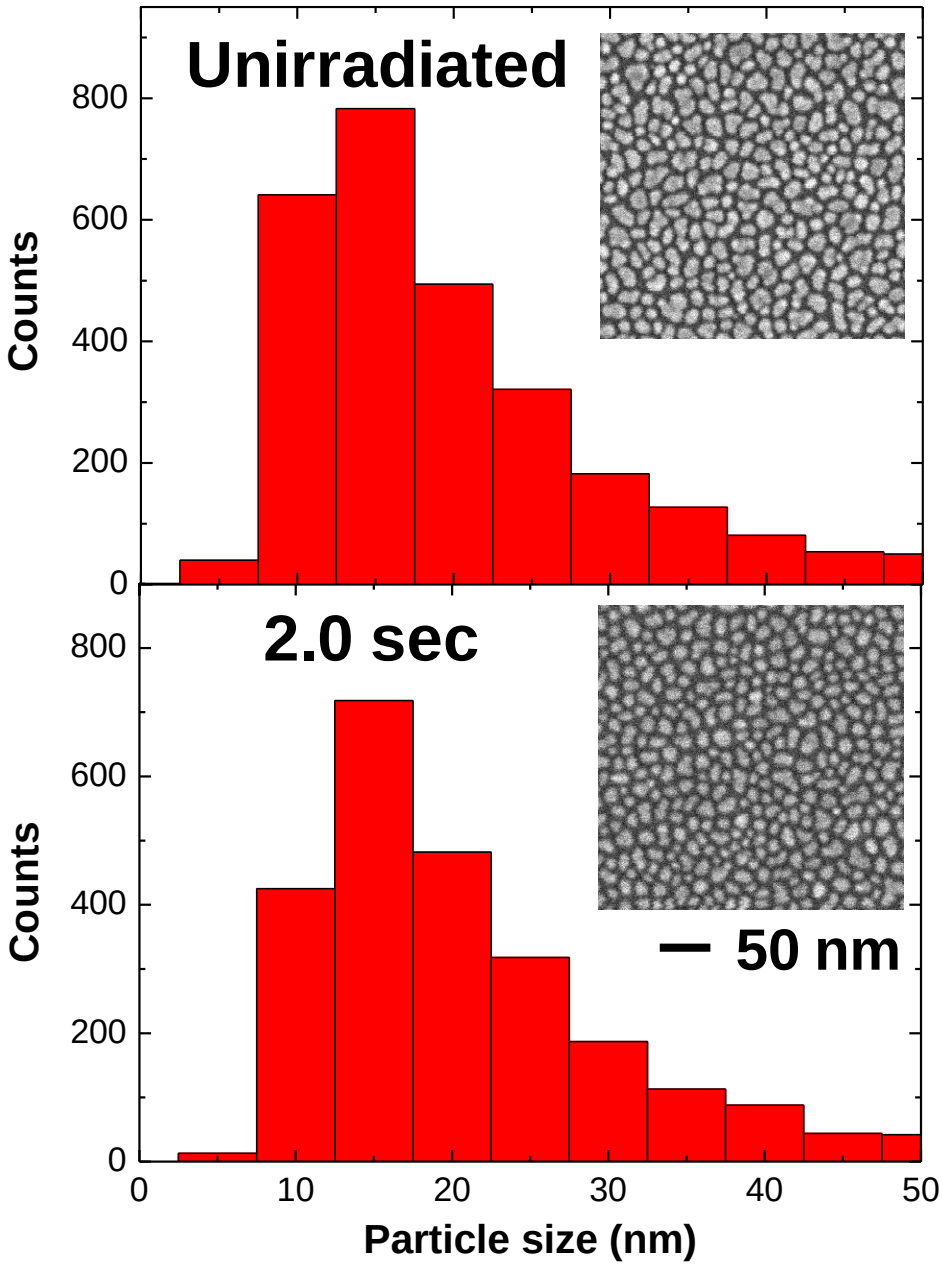

Fig. 3.14: Size distributions of Au NPs before (top) and after (bottom) Ar ion irradiation. Inserts are SEM micrographs.

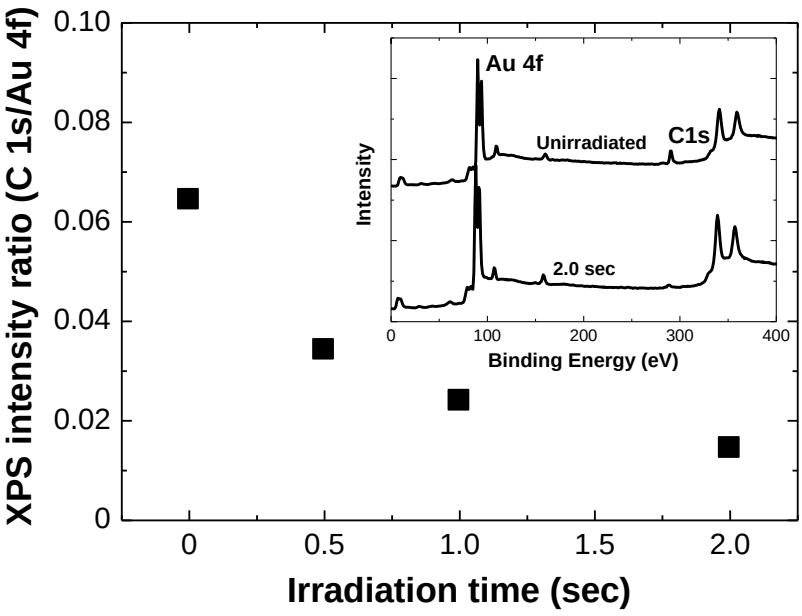

Fig. 3.15: Intensity ratios of C 1*s* /Au 4*f* obtained in XPS measurements as a function of irradiation time. XPS survey scan spectra are included.

3.3.4. Modification of Au nanoparticles by N ion irradiation

As mentioned in Section 3.3.2, N ion irradiation at low fluence leads to a significant increase in optical extinction of Ag NP array. Although the explicit mechanism is unclear, irradiation-induced crystallization may contribute to the extinction increase. The author tried to enhance the extinction by using 350 keV N ions, but observed results belied my expectation as can be seen in Fig 3.16. At present, the origin of difference in N ion irradiation effects between Au and Ag NP arrays is unknown. One possible reason may be the difference in activation energy for crystallization. The author is now surveying the values for Au and Ag.

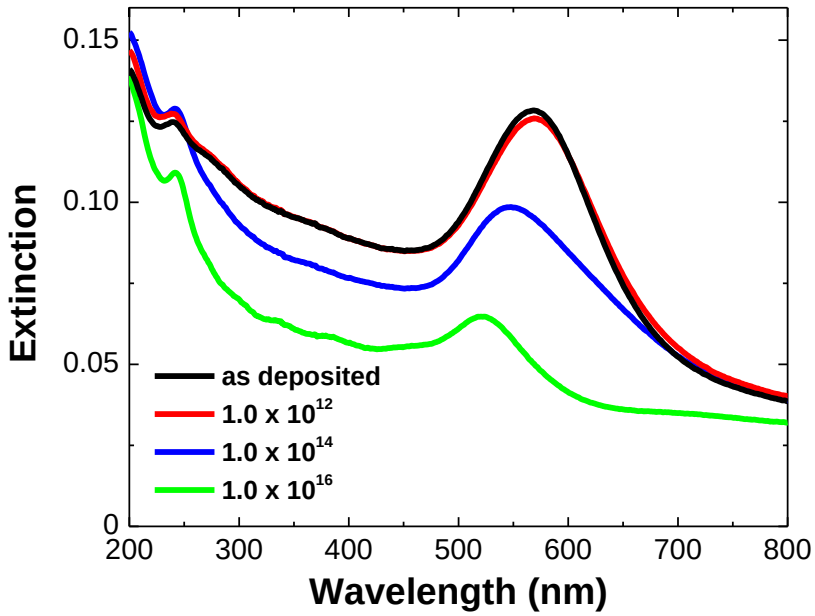

Fig. 3.16: Optical extinction spectra of Au/SiO_2 irradiated with 350 keV N ions. Irradiation fluences are 0, 1.0×10^{12}, 1.0×10^{14}, 1.0×10^{16} N^+/cm^2.

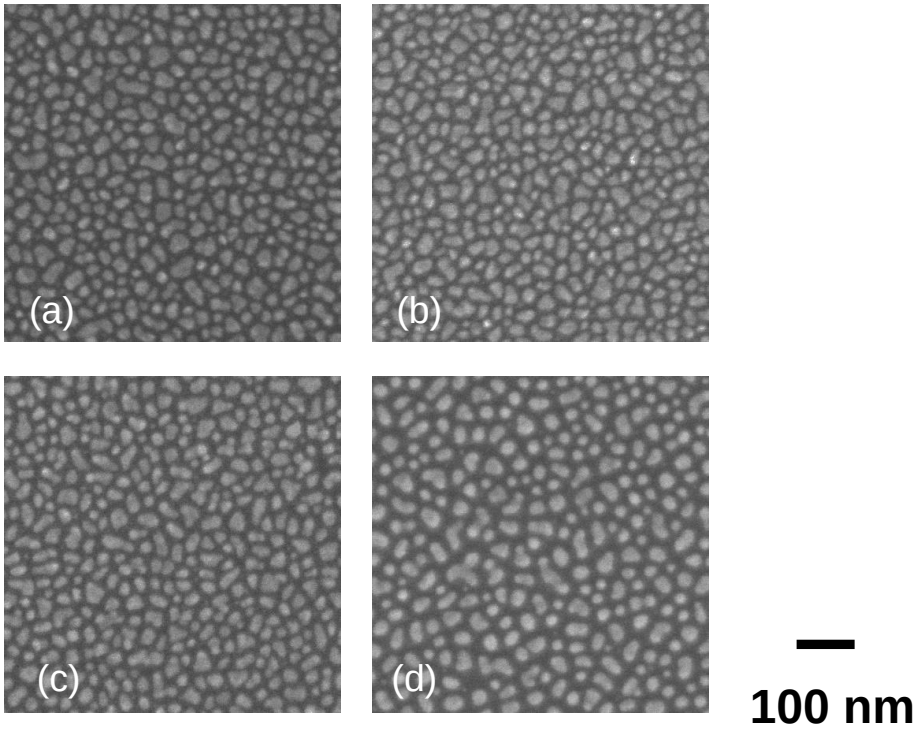

Fig. 3.17: SEM images of Au NPs on SiO_2 samples irradiated with 350 keV N ions. Irradiation fluences are (a) 0, (b)1.0×10^{12}, (c)1.0×10^{14}, (d)1.0×10^{16} N^+/cm^2.

Finally, it is also worth noting that the optical extinction of Au NP array irradiated with N ions to a fluence of 1.0×10^{16} N^{+}/cm^{2} is extremely weak even if half of Au NPs are sputtered away as can be seen in Fig. 3.17. This result suggests that such extinction weakening is largely attributed to the increase in the inter-particle distance.

3. 4. Conclusion

Remarkable changes, blue-shift and narrowing, in localized surface plasmon resonance of Ag NPs without significant morphological modifications have been demonstrated with plasma treatments. The findings provide information on the reason why most of the experimental extinction spectra of the NPs on substrates are considerably different from that calculated by Mie's theory. Further, the obtained results are of importance for sensor applications. A sharp plasmon resonance line is much preferable to a nanoparticle-based sensor, in which a change in optical absorbance at a fixed wavelength is being observed to detect analytes [8]. The degree of the absorbance change, that is sensitivity, depends on the sharpness of the plasmon resonance line; the narrower the line width is, the higher the sensitivity one can

obtain. In addition, high energy N ions are found to enhance LSPR of Ag NP array, probably due to irradiation-induced crystallization.

The author applied plasma exposure as well as ion irradiation to modify Au NPs. In the case of the modification of Au NPs, the remarkable reduction in LSPR intensity due to elimination of carbon impurities as well as the large inter-particle distance was observed, definitely undesirable for plasmonic sensors.

References

[1] N. Lopez, T. V. W. Janssens, B. S. Clausen, Y. Xu, M. Mavrikakis, T. Bligaard, J. K. Nørskov, J. Catal. 2004, **223**, 232.

[2] N. Hanada, T. Ichikawa, H. Fujii, J. Phys. Chem. B 2005, **109,** 7188.

[3] T. Sato, H. Ahmed, D. Brown, B. F. G. Johnson, J. Appl. Phys. 1997, **82**, 696.

[4] B. Mukherjee, M. Mukherjee, Appl. Phys. Lett. 2009, 94, 173510.

[5] S. A. Maier, P. G. Kik, H. A. Atwater, Appl. Phys. Lett. 2002, **81**, 1714.

[6] S. Pillai, K. R. Catchpole, T. Trupke, M. A. Green, J. App. Phys. 2007, **101**, 093105.

[7] A. Kumar, P. K. Vemula, P. M. Ajayan, G. John, Nat. Mater. 2008, 7, 236.

[8] C. S. Cheng, Y. Q. Chen, C. J. Lu, Talanta 2007, **73**, 358.

[9] M. D. Malinsky, K. L. Kelly, G. C. Schatz, R. P. Van Duyne, J. Am. Chem. Soc. 2001, **123**, 1471.

[10] G. Raschke, S. Kowarik, T. Franzl, C. So1nnichsen, T. A. Klar, J. Feldmann, Nano Lett. 2003, **3**, 935

[11] J. C. Riboh, A. J. Haes, A. D. McFarland, C. R. Yonzon, R. P. Van Duyne, J. Phys. Chem. B 2003, **107**, 1772.

[12] A. M. Michaels, J. Jiang, L. Brus, J. Phys. Chem. B 2000, **104**, 11965.

[13] K. Kneipp, Y. Wang, H. Kneipp, L. T. Perelman, I. Itzkan, R. R. Dasari, M. S. Feld, Phys. Rev. Lett. 1997, **78**, 1667.

[14] S. Nie, S. R. Emory, Science 1997, **275**, 1102.

[15] M. H. Lee, P. J. Dobson, B. Cantor, Thin Solid Films 1992, **219**, 199.

[16] G. Xu, M. Tazawa, P. Jin, S. Nakao, Appl. Phys. A, 2005, **80**, 1535.

[17] R. Brahma, M. G. Krishna, Nucl. Inst. Meth. B 2008, **266**, 1493.

[18] T. Donnelly, B. Doggett, J. G. Lunney, Appl. Surf. Sci. 2006, **252**, 4445.

[19] H. Hövel, S. Fritz, A. Hilger, U. Kreibig, M. Vollmer, Phys. Rev. B 1993, **48**, 18178.

[20] N. Hashimoto, Y. Yamamoto, S. Niijima, e-J. Surf. Sci. Nanotech. 2005, **3**, 120.

[21] B. K. Russell, J. G. Mantovani, V. E. Anderson, R. J. Warmack, T. L. Ferrell, Phys. Rev. B 1987, **35**, 2151.

[22] K. L. Kelly, E. Coronado, L. L. Zhao, G. C. Schatz, J. Phys. Chem. B 2003, **107**, 668.

[23] G. W. Arnold, J. A. Borders, J. Appl. Phys. 1977, **48**, 1488.

[24] M. D. Mcmahon, R. Lopez, H. M. Meyer, L. C. Feldman, R. F. Haglund, Appl. Phys. B 2005, **80**, 915.

[25] R. Jin, Y. W. Cao, C. A. Mirkin, K. L. Kelly, G. C. Schatz, J. G. Zheng, Science 2001, **294**, 1901.

[26] J. Schwan, S. Ulrich, V. Batori, H. Ehrhardt, S. R. P. Silva, J. Appl. Phys. 1996 **80**, 440.

[27] A. Kudelski, Chem. Phys. Lett. 2006, **427**, 206.

[28] T. Okamoto, in Near-Field Optics and Surface Polaritons, ed. by S. Kawata, Topics in Applied Physics Vol. 81 (Springer-Verlag, Berlin, 2001), p. 111.

[29] K. Kawaguchi, M. Saito, K. Takahiro, S. Yamamoto, and M. Yoshikawa, Plasmonics 2011, **6**, 535.

Chapter 4

Plasmonic cyclohexane-sensing by sputter-deposited Au nanoparticle array on SiO_2

1. Introduction

Hydrogen fuel cells, which can be a clean energy source to convert chemical energy into electrical energy by direct reaction of H_2 and O_2 without emitting CO_2 [1], are being developed for vehicles to reduce environmental pollutant emission. In the fuel cell-driven vehicles, the safety storage and transportation of hydrogen are the most important issues to be realized. Compressed H_2 gases, liquid hydrogen and metal hydrides can be a hydrogen source to be supplied into the fuel cell mounted on such vehicles. It is challenging for engineers to develop a light and tough storage tank that meets requirements for a long range safety driving. An alternative option is to store hydrogen containing compounds, such as gasoline or methanol, onboard a vehicle and extracting the hydrogen through dehydrogenation (using a fuel reformer). Of these hydrogen-containing compounds, cyclohexane C_6H_{12}, which is in liquid phase at ordinary temperatures and pressures like gasoline, is known to have extremely high hydrogen content in weight and volume [2,3]. The conventional infrastructures, e.g. gas stations constructed for gasoline-driven vehicles, can be utilized to store and supply cyclohexane, which is an advantage over the other hydrogen sources. Cyclohexane is a highly flammable volatile organic compound (VOC): its explosive limit is as low as 1.3 vol% [4] in air. One must, therefore, take care the leakage of cyclohexane in a vehicle. Thus the small amount of cyclohexane should be detected as quickly as possible.

Many works for the detection of VOCs using semiconductor-type gas sensors, including SnO_2 [5−7], TiO2 [7−9] WO3 [10,11] and ITO [12], have been reported. For these sensors in which the change in resistivity is measured, it is necessary to heat up to 300−400 °C, higher than the ignition point of cyclohexane (246 °C [4]). Such sensors are, therefore, inapplicable to the safe detection of cyclohexane. The method via an optical technique, e.g. gas-chromic of WO_3 [13] upon hydrogen exposure, is a candidate for the safe detection, although it is not a straightforward approach because hydrogen must be extracted from VOCs by using an appropriate catalyst at elevated temperature. There is an alternative optical technique via localized surface plasmon resonance (LSPR) of Ag and Au nanoparticles (NPs), in which the change in optical absorption upon arrival of VOC molecules is measured. The intense LSPR band is located in the visible range for Ag and Au NPs [14]. The characteristic of LSPR band, intensity and wavelength, depends on a particle size [15,16], a shape [17−19], a distance between particles [20] and a refractive index of the surrounding medium [14,21,22]. Such dependences enable one to apply the NPs to chemical and biological sensors [23−26]. Cheng et al. [27], for example, measured optical absorption to detect VOCs such as toluene using Au and Ag NPs. Of VOCs, cyclohexane has a large refractive index (n_D = 1.426 [4]), which is distinguishable from air (n_D = 1.000 [4]) as well as water vapor (n_D = 1.000 [4]) and therefore would be favorable for detecting it by the use of optical absorption measurements.

To date, most of the Au or Ag NPs have been synthesized by wet processes, e.g metal colloidal chemical methods as has been applied by Cheng et al. [27]. As mentioned above, the characteristic of the LSPR band is dependent on the inter-particle distance: the band intensity becomes stronger with decreasing the distance. Thus a high sensitive detection of VOCs requires a high density of Au or Ag NPs on a substrate. It is, however, difficult to prepare such close-packed Au or Ag NPs on a substrate by the wet processes. Moreover, the wet processes will leave chemical residues on NP surfaces, lowering detection sensitivity for VOCs. Alternatively, dry processes such as magnetron sputtering and pulse laser ablation deposition methods are applicable to fabricate densely arranged clean Au or Ag NP arrays on a substrate [28−33]. In these methods, the density and morphology of an array of NPs can be easily controlled by adjusting preparation parameters, including power, irradiation time, substrate temperature, and so on, to obtain high detection sensitivity for VOCs.

In this chapter, the author focuses my attention on detecting cyclohexane vapor by the LSPR of Au NPs. The present objective is to find out optimum conditions for the preparation of an Au NP array on SiO_2 substrates as a plasmonic sensor for cyclohexane whose concentration is lower than its explosion limit of 1.3 vol%.

2. Experimental methods

Au NPs on SiO_2 and Si substrates were fabricated by an rf magnetron sputtering method. The base pressure of a sample preparation chamber was ~ 6×10^{-5} Pa. Ar gas was introduced into the chamber to a pressure of 3.6×10^{-2} Pa. The Au disc target (99.99 %) was sputtered by the Ar plasma at a power of 5 W. The SiO_2 glasses ($10 \times 10 \times 0.5$ mm^3) cleaned by using ethanol were used as the transparent substrate for optical sensing. Au NPs were also deposited on polished Si wafers with a native oxide layer for Rutherford backscattering spectrometry (RBS) and scanning electron microscope (SEM) in order to avoid electric charging. During the deposition, the substrates were heated up to 200−400 °C to obtain isolated Au NPs. The areal density of Au atoms on substrates was determined with RBS employing a 2.0 MeV He^+ ion beam. A He^+ ion beam with a spot size of 1.0 mm in diameter was provided by a 3.0 MV single ended accelerator at JAEA Takasaki. The backscattered He ions were detected by using a surface barrier detector placed at an angle of 165° with respect to the beam. The RBS analysis revealed that the Au areal densities were $1.1 - 7.1 \times 10^{16}$ Au atoms/cm^2. The deposition rate was estimated to be ~ 0.6 nm/min from the Au areal density and deposition time. The surface morphology of the Au NPs was observed by the field emission SEM operating at an acceleration voltage of 15 kV. The crystalline form of the Au NPs was confirmed by θ-2θ scans of X-ray diffraction (XRD) analysis using Cu Kα (λ = 0.1542 nm) radiation.

The LSPR sensor experiment was performed by the setup which was essentially the same as the one presented by Malinsky et al. [26]. UV-Vis extinction spectra of the Au NPs were measured using a compact spectrometer (USB-4000, Ocean Optics) in the wavelength range between 450 and 800 nm. The unpolarized light from a tungsten-halogen light source was incident normal to the sample surface through a quartz optical fiber. Cyclohexane gas mixed with high purity N_2 gas was flowed over the Au NPs at a constant flow rate of 100 sccm at room temperature. The concentration of cyclohexane gas was measured by a Fourier transform infrared (FTIR) spectrometer (Perkin-Elmer, Spectrum One) equipped with a gas cell and a mercury cadmium telluride detector, which was calibrated with a known cyclohexane concentration. The concentration of cyclohexane gas was varied from 0.5 to 5 vol% by adjusting the flow ratio between saturated cyclohexane and N_2 gas flow. The concentration of water vapor in ambient air was measured by a moisture analyzer (Hygro-3M with D-2 detector, General Eastern Co. Ltd.). The response of Au NPs to cyclohexane molecules was recognized by the change in LSPR intensity before and after 5 minute-exposure of dilute cyclohexane vapor.

3. Results and discussion

Firstly, typical extinction spectra of Au NP arrays deposited on SiO_2 substrates prepared at a temperature of 300 °C for various deposition times are presented to discuss feature of each spectrum. Fig. 4.1 shows the optical extinction spectra of the samples. The Au areal densities determined by RBS for three samples corresponding to (a), (b) and (c) are 1.1×10^{16}, 4.4×10^{16} and 7.1×10^{16} Au atoms/cm^2, respectively. The characteristics of an LSPR peak located at 500−600 nm, including peak position, width and intensity, strongly depend on the Au areal density. The peak position gradually changes from 560 to 660 nm, so-called "red-shift", and both the peak width and the extinction increases as the Au areal density increases. The increase in the extinction can be simply explained by the increased number of Au NPs. As shown in Fig. 4.2, which is a set of simulated optical density generated from MQAggr software (Michael Quinten, Wissenschaftlich-technische Software), the peak position and optical density are sensitive to the inter-particle spacing l_{gap} rather than the diameter d of an individual Au NP. The inter-particle coupling effects occur when NPs are closely spaced. The dipole field from LSPR of an Au NP can induce plasmon oscillation in other neighboring Au NPs via near-field electrodynamic interactions. For elliptical Au NPs, in fact, Su et al. [20] have experimentally showed that plasmon resonant peak is significantly shifted to higher wavelength as the inter-particle spacing is reduced. In my Au NP aggregates, inter-particle spacing decreases as

the deposited number of Au atoms, i.e., the Au areal density increases because the number of Au NPs and/or the particle size becomes larger, resulting in the red-shift. A contribution of reflection to the extinction spectrum at wavelengths exceeding 700 nm becomes significant for densely arranged Au NP arrays, like a continuous Au thin film. The contribution of reflection broadens the peak and increases extinction at that wavelength region, which would be unfavorable for optical gas sensing materials.

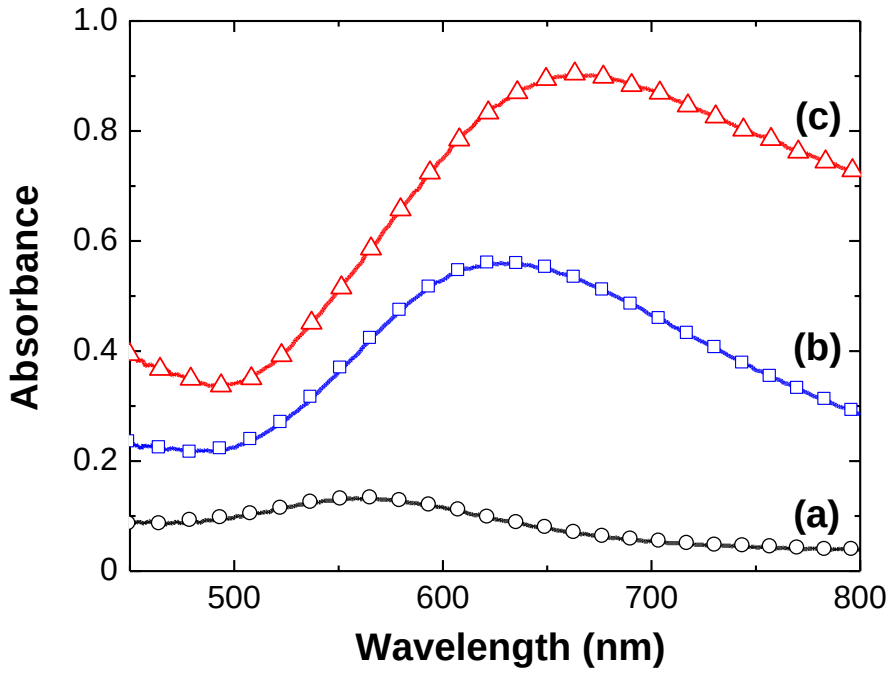

Fig. 4.1: The optical extinction spectra of samples prepared with three different Au areal densities. The Au areal densities for (a), (b) and (c) are 1.1×10^{16}, 4.4×10^{16} and 7.1×10^{16} Au atoms/cm^2, respectively. The deposition temperature for the samples is kept at 300 °C.

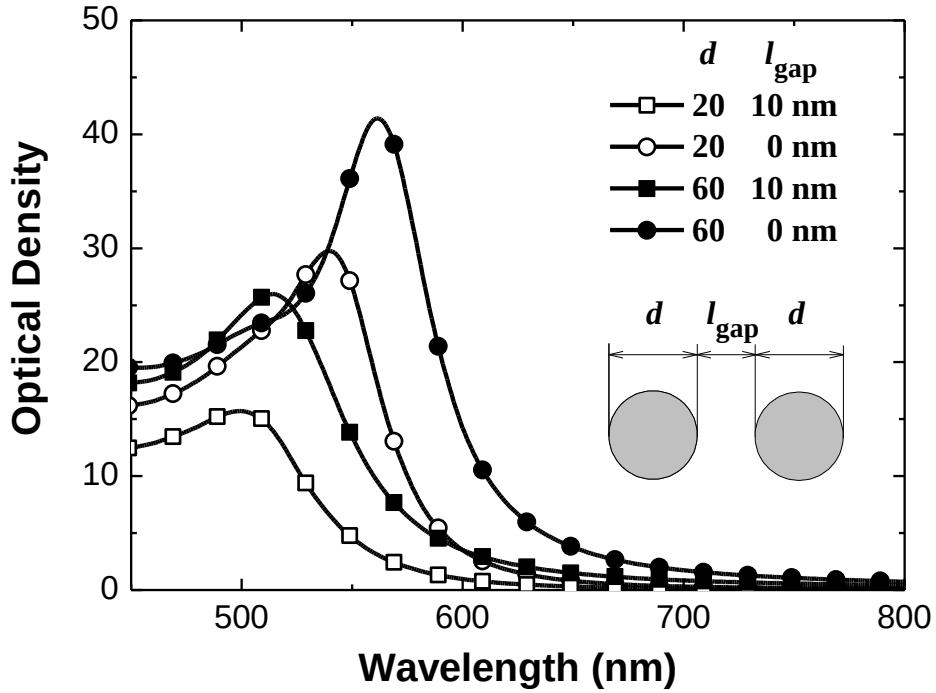

Fig. 4.2: The simulated spectra shown by optical density of a pair of two Au NPs with diameter *d* and interparticle spacing *l*sp. The combinations of *d* and *l*sp are 20, 10 nm for open squares (□), 20, 0 nm for open circles (○), 60, 10 nm for filled squares (■) and 60, 10 nm for filled circles (●).

Secondly, the response of an extinction spectrum of Au NPs against cyclohexane is examined as functions of an Au areal density and a deposition temperature. Fig. 4.3 (a) shows the typical extinction spectra of the sample prepared at 300 °C before and after exposure of 5 vol% cyclohexane gas. The Au areal density of the sample is 4.4×10^{16} Au atoms/cm^2. The extinction peak due to LSPR becomes intense and the resonance peak position shifts toward longer wavelength after the gas exposure. The observed change in the extinction spectrum can

be understood by the alteration of a refractive index of the surrounding medium for Au NPs after the gas flow. The extinction difference is defined as summing all differences in intensity over wavelengths from 500 to 800 nm between gas-exposed and unexposed spectra, as is shown by hatched area in Fig. 4.3 (a). Hereafter the extinction difference is used as a signal for the detection of cyclohexane. In Fig. 4.3 (b), the extinction difference is plotted against an Au areal density of a sample prepared at 200 or 300 °C. The Au areal density at which the maximum difference occurs is found to be 4.4×10^{16} Au atoms/cm^2 both for the deposition temperature of 200 and 300 °C. As mentioned above, for samples prepared with higher Au areal densities, e.g., 7.1×10^{16} Au atoms/cm^2, a contribution of scattering to the extinction spectrum becomes significant at wavelengths exceeding 700 nm, leading to a reduction in the sensitivity. Furthermore, for all the Au areal densities, the sensitivity of a sample deposited at 300 °C is expected to be higher than that of a sample deposited at 200 °C. Then the Au areal density is fixed at 4.4×10^{16} Au atoms/cm^2 to examine the deposition temperature dependence of the extinction difference. Fig. 4.3 (c) depicts the extinction differences plotted as a function of deposition temperature for a sample prepared with 4.4×10^{16} Au atoms/cm^2. The extinction difference increases until the deposition temperature reaches 300 °C, and then decreases beyond that temperature, indicating that the highest sensitivity for cyclohexane is obtained for a sample prepared by heating at 300 °C during deposition.

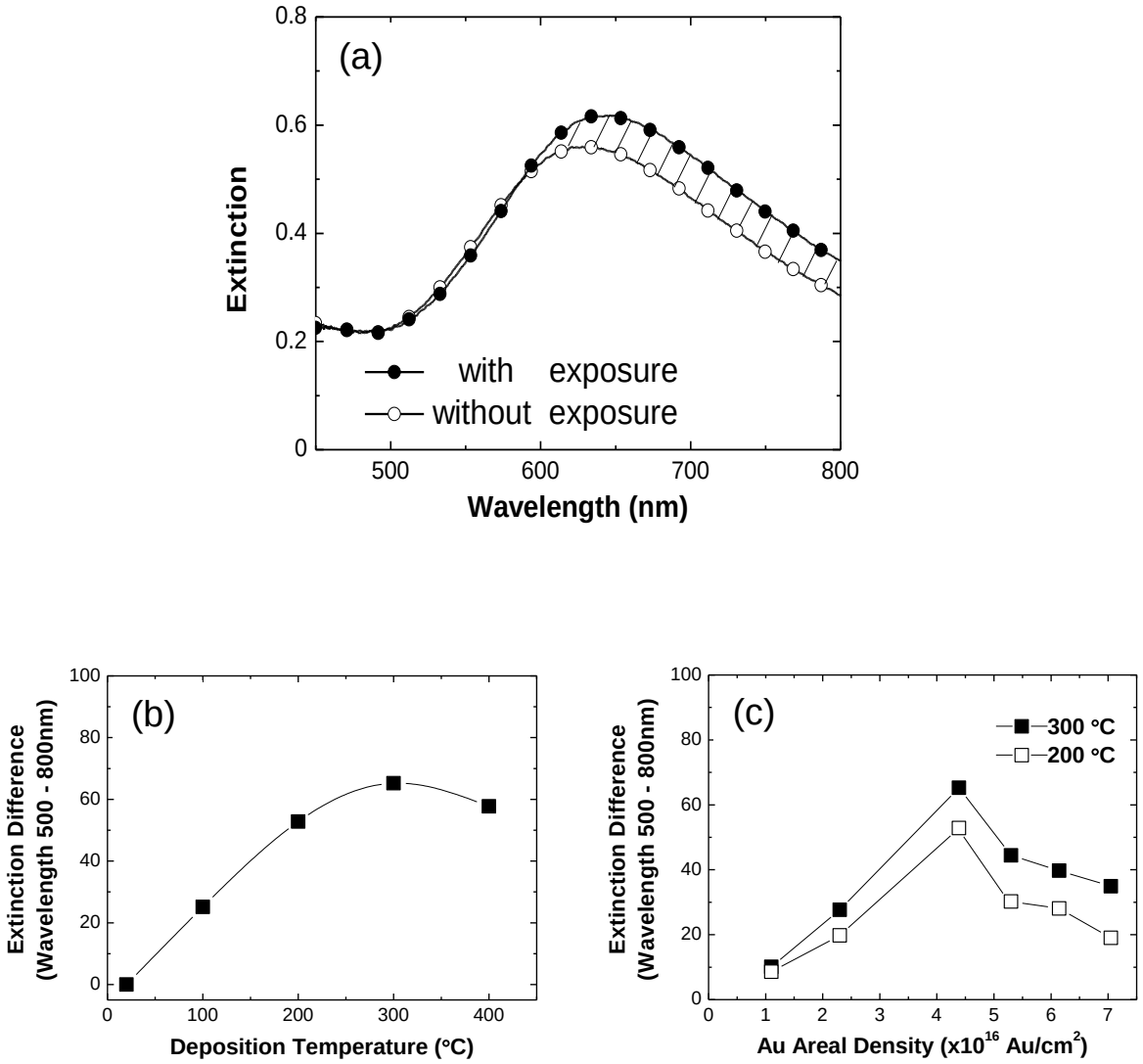

Fig. 4.3: The optical extinction spectra of the Au NP array on SiO2 prepared with 4.4×10^{16} Au atoms/cm^2 at 300 °C before (○) and after (●) exposure of 5 vol% cyclohexane gas (a). The hatched area represents the extinction difference defined as summing all differences in intensity over wavelengths from 500 to 800 nm between gas-exposed and unexposed spectra. The extinction differences are plotted against an Au areal density (b) and deposition temperature (c). The deposition temperature of 200 or 300 °C are indicated by open squares (□) and filled squares (■), respectively, in the figure (b). The Au areal density of the sample is 4.4×10^{16} Au atoms/cm^2 in the figure (c).

Next, the surface morphology and crystal structure are characterized for the sample expected to possess the highest sensitivity for cyclohexane, i.e., Au NP array prepared with 4.4 × 10^{16} Au atoms/cm^2 at a temperature of 300 °C. For SEM observations a single-crystalline Si was used as a substrate. It should be noted that the surface of the Si substrate is covered by a native oxide, meaning that the Au NPs are deposited onto SiO_2/Si. A SEM image reveals densely arranged but isolated Au NPs with sizes 10–60 nm, as shown in Fig. 4.4 (a). The morphology of the Au NPs is not spherical or spheroidal but truncated polygonal. The particle size distribution is measured as shown in Fig. 4.4 (b), assuming that Au NPs are spherical. A logarithmic-normal (lognormal) size distribution is often observed for NPs as a result of random nucleation and growth [34,35], so that

$$n_i(d_i) = \frac{1}{\sqrt{2\pi}\sigma d_i} \exp\left\{ -\frac{\left(\ln d_i - \ln d_{\mathrm{m}}\right)^2}{2\sigma^2} \right\}$$

where d_{m} represents the mean particle diameter and σ is the standard deviation of the distribution $n_i(d_i)$. Fitting a lognormal curve to the size distribution results in d_{m} = 30 nm and σ = 0.34. The particle density is roughly estimated to be 1.1 × 10^{11} Au NPs/cm^2.

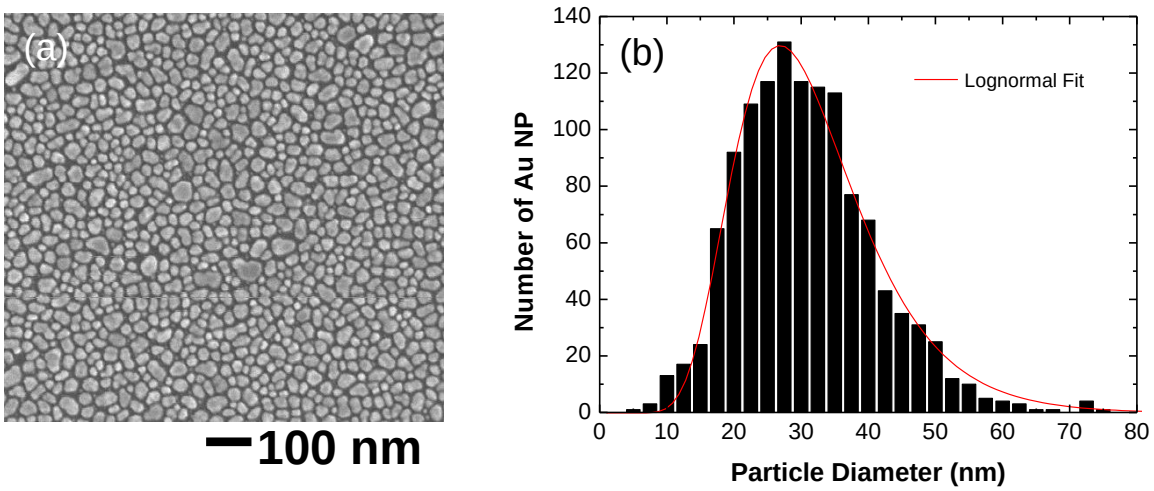

Fig. 4.4: A SEM image of the sample prepared with 4.4×10^{16} Au atoms/cm^2 at 300 °C (a) and the size distribution of Au NPs in the sample (b). A lognormal fitting curve is also presented in the figure (b).

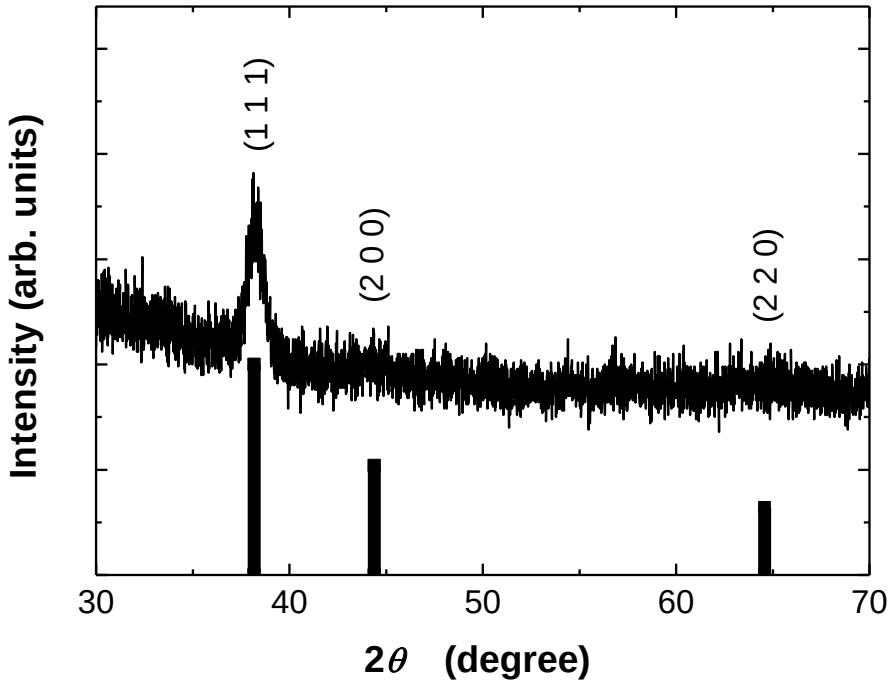

Fig. 4.5: XRD patterns of the sample prepared with 4.4×10^{16} Au atoms/cm^2 at 300 °C (line) and the fcc metallic Au reference taken from JCPDS 65-2870 (bars)

Figure 4.5 shows an XRD pattern taken from the Au NP array on a SiO_2 substrate prepared with 4.4×10^{16} Au atoms/cm^2 at a temperature of 300 °C. This pattern is compared with that of Au reference (JCPDS 65-2870). The line located at $2\theta = 38.2°$ corresponds to the (111) plane of the face-centered-cubic (fcc) Au ($d_{111} = 0.2355$ nm). The d_{111} spacing of the Au NP array is calculated to be 0.235 nm, which is in good agreement with that of the fcc Au, but the pattern for the present Au NP array consists of one prominent line in the 2θ region between 30° and 70°, quite different from that for the randomly oriented fcc Au crystallites. The pattern observed here indicates that most of the Au NPs have the same [111] orientation parallel to the surface normal. The preferentially [111] oriented Au crystallites tend to form because the Au (111) surface has the lowest surface energy [36,37]. In fact, Ino and Ogawa [38] found that Au particles evaporated under UHV condition took (111) orientation.

In the XRD pattern of the Au NP array, a width of the (111) line is found to be 1.7×10^{-2} rad, which is much larger than the instrumental line broadening of 1.5×10^{-3} rad, indicating that individual Au NPs are very thin. The thickness of the Au NPs can be estimated by using Scherrer's formula [39,40] to be 8.5–9.5 nm, depending on Scherrer constant K (0.9 – 1.1). The Au areal density of 4.4×10^{16} Au atoms/cm^2 corresponds to the ideal film thickness of 7.5 nm, assuming that the film is uniformly continuous and the surface coverage is unity. The surface coverage can be deduced by the ratio of the ideal thickness (7.5 nm) to the thickness estimated by XRD (8.5 – 9.5 nm). The ratio yields the surface coverage of 0.8–0.9. This result means that Au NPs are arranged closely, consistent with the SEM image of Au NP array deposited on Si substrate with a native oxide layer (Fig. 4.4 (a)).

Finally, the detection limit of the densely arranged Ag NP array (4.4×10^{16} Au atoms/cm^2, 300 °C) for cyclohexane is estimated by measuring the optical response to cyclohexane with reduced concentrations. The cyclohexane concentrations are plotted against extinction difference between gas-exposed and unexposed spectra, as shown in Fig. 4.6. Even at cyclohexane concentration of 0.5 vol%, which is approximately one third of its explosion limit (1.3 vol%), the amount of extinction difference is measurable (~ 4). The detection limit for cyclohexane can be roughly estimated by the extrapolation method. The author tries to find a quadratic function $y = ax^2 + bx + c$ that best fits a given set of data, where variables x and y represent the extinction difference and cyclohexane concentration, respectively. The constant term c obtained is 0.305, suggesting that the amount of extinction difference goes down to zero at a cyclohexane concentration of ~ 0.3 vol%, which is, in principle, the detection limit for cyclohexane. The estimated detection limit of ~ 0.3 vol% is lower than one fourth of explosion limit of cyclohexane.

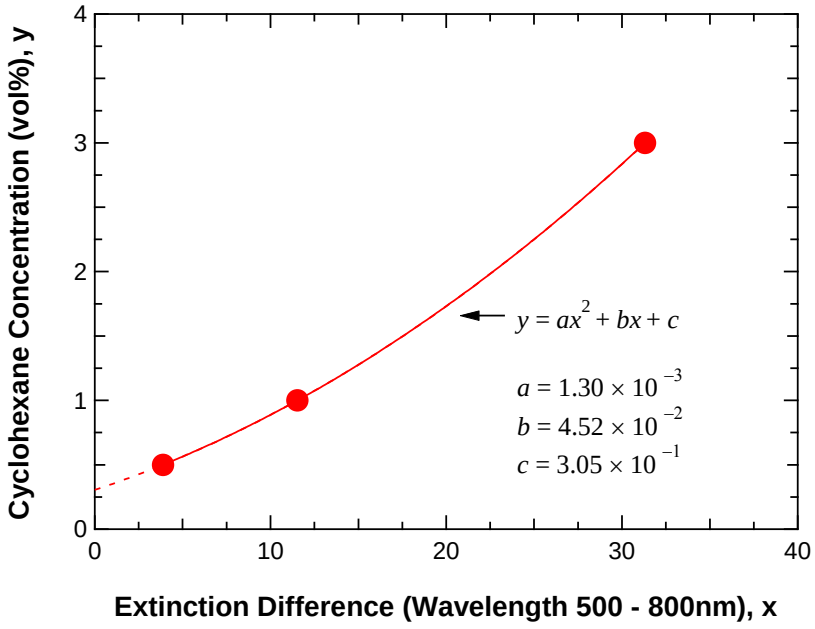

Fig. 4.6: The cyclohexane concentrations plotted against extinction difference between gas-exposed and unexposed spectra (filled circles) for the sample prepared with 4.4×10^{16} Au atoms/cm^2 at 300 °C and a fitting curve as the form of a quadratic function $y = ax^2 + bx + c$, where variables x and y represent the extinction difference and cyclohexane concentration, respectively

4. Conclusion and outlook

Plasmonic Au NP arrays on SiO_2 have been fabricated to detect dilute cyclohexane by a sputter deposition technique. The increase in refractive index of the surrounding medium for the Au NP array upon exposure of cyclohexane vapor changes both the peak position and intensity in its extinction spectrum in the wavelength range of 500−800 nm, which enables one to detect it. The highest sensitivity was obtained in the case of the Au NP array prepared with

4.4×10^{16} Au atoms/cm^2 at a deposition temperature of 300 °C. The Au NPs, whose mean diameter was 30 nm, were densely arranged in the sample. The surface coverage has been roughly estimated to be 0.8–0.9 by XRD analysis. Furthermore, the preferentially [111] oriented Au NPs, which are normal to the substrate surface, have been observed in the sample. By using such a plasmonic Au NP array on SiO_2, the detectable concentration of cyclohexane has been estimated experimentally to be 0.5 vol%, and computationally to be ~ 0.3 vol%, much lower than its explosion limit (1.3 vol%).

In the present work, the author tried to find an optimum condition for preparing a plasmonic Au NP array on SiO_2 with the highest sensitivity for cyclohexane. The sensing of cyclohexane must be done as quickly as possible in a vehicle for the next generation. The shape and size of a cell in which the plasmonic Au NP sensor is installed are the most important factors to determine the response time. Our laboratory member is now designing the cell for a prompt sensing of cyclohexane.

References

[1] Steel BCH, Heinzel A, Nature 2001, **414**, 345

[2] Kariya N, Fukuoka A, Utagawa T, Sakuramoto M, Goto Y, Ichikawa M, Appl Catal. 2003, **247**, 247

[3] Okada Y, Sasaki E, Watanabe E, Hyodo S, Nishijima H, J. Hydrog. Energy 2006, **31**, 1348

[4] Lide DR (1990) CRC handbook of chemistry and physics.

[5] Srivastava AK, Sens. Actuator B 2003, **96**, 24

[6] Sakai Y, Kadosaki M, Matsubara I, Itoh T, J. Ceram. Soc. Jpn. 2009, **117**, 1297

[7] Wen Z, Tian-mo L, Physica B, 2009, **405**, 1345

[8] Seo M-H, Yuasa M, Kida T, Huh J-S, Yamazoe N, Shimanoe K, Sens. Actuator B, 2005, **137**, 513

[9] Seo M-H, Yuasa M, Kida T, Huh J-S, Yamazoe N, Shimanoe K, Sens. Actuator B, 2011, 154, 251

[10] Kanda K, Maekawa T, Sens. Actuator B, 2005, **108**, 97

[11] Righettoni M, Tricoli A, Patsinis SE, Chem. Mater. 2010, **22**, 3152

[12] Vaishanv VS, Patel PD, Patel NG, Mater. Manuf. Process, 2006, **21**, 257

[13] Yoshimura K, Hakoda T, Yamamoto S, Yoshikawa M, J. Phys. Chem. Sol. 2012, **73**, 696

[14] Kreibig U, Vollmer M, *Optical properties of Metal Clusters*. (Springer, Berlin, 1995)

[15] Link S, El-Sayed MA, J. Phys. Chem. B, 1999, **103**, 4212

[16] Nath N, Chikoti A, Anal. Chem. 2004, **76**, 5370

[17] Warshavski O, Minai L, Bisker G, Yelin D, J. Phys. Chem. C, 2011, **115**, 3910

[18] Rotello VM, *Nanoparticles: building blocks for nanotechnology*. (Kluwer, New York, 2004)

[19] Nehl CL, Liao H, Hafner JH, Nano. Lett. 2006, **6**, 683

[20] Su KH, Wei QH, Zhang X, Mock JJ, Smith DR, Schultz S, Nano. Lett. 2003, **3**, 1087

[21] Okamoto T, Yamaguch I, Kobayashi T, Opt. Lett. 2000, **25**, 372

[22] Mock JJ, Smith DR, Schultz S, Nano. Lett. 2003, **3**, 485

[23] Riboh JC, Haes AJ, McFarland AD, Yonzon CR, Van Duyne RP, J. Phys. Chem, B, 2003, **107**, 1772

[24] Haes AJ, Zou S, Schatz GC, Van Duyne RP, J. Phys. Chem. B, 2004, **108**, 6961

[25] Spadavecchia J, Prete P, Lovergine N, Tapfer L, Rella R, J. Phys. Chem. B, 2005, **109**, 17347

[26] Malinsky MD, Kelly KL, Schatz GC, Van Duyne RP, J. Am. Chem. Soc. 2001, **123**, 1471

[27] Cheng C-S, Chen Y-Q, Lu C-J, Talanta, 2007, **73**, 358

[28] Warmack RJ, Humphrey SL, Phys. Rev. B, 1986, **34**, 2246

[29] Russell BK, Mantovani JG, Anderson VE, Warmack RJ, Ferrell TL, Phys. Rev. B, 1987, **35**, 2151

[30] Granqvist CG, Handeri O, Solid. State. Commun. 1976, **19**, 939

[31] Zhou X, Wei Q, Sun K, Wang L, Appl. Phys. Lett. 2009, **94**, 133107

[32] Zuo J, Appl. Surf. Sci. 2010, **256**, 7096

[33] Wei H, Eilers H, J. Phys. Chem. Solids, 2009, **70**, 459

[34] Kurtz SK, Carpay FMA, J. Appl. Phys. 1980, **51**, 5725

[35] Bergmann RB, Bill A, J. Cryst. Growth, 2008, **310**, 3135

[36] Shim JH, Lee BJ, Cho YW, Surf. Sci. 2002, **512**, 262

[37] Baskes MI, Phys. Rev. B, 1992, **46**, 2727

[38] Ino S, Ogawa S, J. Phys. Soc. Jpn. 1967, **22**, 1365

[39] Cullity BD, *Elements of X-ray Diffraction*. (Addison-Wesley, Reading MA, 1978)

[40] Eberhart JP, *Structure and Chemical Analysis of Materials*. (Wiley, Chichester, 1991)

Chapter 5

Summary and concluding remarks

Plasmonic nanoparticles made of silver and gold exhibit unique optical properties due to localized surface plasmon resonance in the visible wavelength range. A plasmonic sensor is one of the most useful applications of such nanoparticles. In this thesis, energetic ion processes including ion implantation, sputtering and plasma cleaning were utilized to fabricate and modify silver or gold nanoparticle arrays for sensing applications. General introduction, in chapter 1, dealing with optical properties of Ag and Au NPs, application of plasmonic sensor and analytical tools was followed by three chapters except for this chapter

Chapter 2 describes the method to fabricate well-ordered and densely arranged Ag NPs embedded in a thermally grown SiO_2 by implanting with Ag ions to fluences of $0.37-1.2\times10^{17}$ ions/cm^2 at a current density of ~4 μA/cm^2. Cross-sectional transmission electron microscopy and scanning transmission electron microscopy reveal the presence of a two-dimensional array of Ag nanoparticles of 25−40 nm in diameter located at a depth of ~130 nm, together with the self-organization of δ-layer of tiny Ag nanoparticles aligned along the SiO_2/Si interface. X-ray photoelectron spectroscopy and x-ray diffraction confirm the stability of these Ag nanoparticles against oxidation and sulfidation when stored in ambient air for 19−21 months. The SiO_2 substrates including such Ag nanoparticles can be used as stable SERS substrates after removing SiO_2 top layers. Tiny Ag NPs aligned along the SiO_2/Si

interface are expected to exhibit Coulomb Blockade when SiO_2 top layers including irregularly arranged larger Ag nanoparticles are removed appropriately.

In chapter 3, a sputter deposition technique to prepare densely arranged Ag and Au NPs which posse a good plasmonic characteristic was presented and then plasma exposure was applied for cleaning the NP arrays. Plasma treatments of Ag NPs were found to bring about blue-shift and narrowing in their localized surface plasmon resonance. The findings provide information on the reason why most of the experimental absorption spectra of the NPs on substrates are considerably different from that calculated by Mie's theory. Further, the obtained results are of importance for sensor applications. A sharp plasmon resonance line is much preferable to a nanoparticle-based sensor, in which a change in optical absorbance at a fixed wavelength is being observed to detect analytes. The degree of the absorbance change, that is sensitivity, depends on the sharpness of the plasmon resonance line; the narrower the line width is, the higher the sensitivity one can obtain. The author found that the plasmonic properties of Au NPs were also altered by energetic ion irradiation and plasma exposure. In the case of the modification of Au NPs, the remarkable reduction in LSPR intensity due to elimination of carbon impurities was observed, definitely undesirable for plasmonic sensors.

In chapter 4, the plasmonic sensing ability of gold nanoparticle for dilute

cyclohexane was examined. Plasmonic Au NP arrays on SiO_2 have been fabricated to detect dilute cyclohexane by a sputter deposition technique. The increase in refractive index of the surrounding medium for the Au NP array upon exposure of cyclohexane vapor changes both the peak position and intensity in its extinction spectrum in the wavelength range of 500−800 nm, which enables one to detect it. The highest sensitivity was obtained in the case of the Au NP array prepared with 4.4×10^{16} Au atoms/cm^2 at a deposition temperature of 300 °C. The Au NPs, whose mean diameter was 30 nm, were densely arranged in the sample. The surface coverage has been roughly estimated to be 0.8 – 0.9 by XRD analysis. Furthermore, the preferentially [111] oriented Au NPs, which are normal to the substrate surface, have been observed in the sample. By using such a plasmonic Au NP array on SiO_2, the detectable concentration of cyclohexane has been estimated experimentally to be 0.5 vol%, and computationally to be ~ 0.3 vol%, much lower than its explosion limit (1.3 vol%). In the present work, the author tried to find an optimum condition for preparing a plasmonic Au NP array on SiO_2 with the highest sensitivity for cyclohexane. The sensing of cyclohexane must be done as quickly as possible in a vehicle for the next generation. The shape and size of a cell in which the plasmonic Au NP sensor is installed are the most important factors to determine the response time. In our laboratory, we are now designing the cell for a prompt sensing of

cyclohexane.

Finally, the author describes inevitable problems concerning with sulfidation frequently occurred on Ag NPs. Ag is widely known to corrode or tarnish in air by chemical reaction with reduced-sulfur gases such as hydrogen sulfide (H_2S) and carbonyl sulfide (OCS) to form silver sulfide (Ag_2S). Evaporated Ag films stored in normal laboratory air (measured concentrations of H_2S and SO_2 less than 0.2 ppb) developed a film of Ag_2S tarnish whose thickness was 0.1 nm after 1 h, 0.3−0.6 nm after 1 day, 1.5−3 nm after 1 week, and over 6 nm after 1 month. Corrosion of Ag is pronounced at the nanometer scale because of the high surface-to-volume ratio.

As mentioned in chapter 1, the instability of T-LSPR sensors is a source of concern. To obtain Ag NP arrays with stable and reproducible optical properties, depositing an ultrathin silica layer (1.5 nm thick) on Ag NPs is expected to be an effective method. Very recently, our laboratory found that silica layer was deposited by prolonged plasma exposure in a vacuum chamber made of SiO_2. Thus, such plasma exposure will be useful for silica deposition as well as cleaning of Ag NPs. In near future, a stable T-LSPR sensor will be based on the plasma-processed Ag NP array.

List of publications

Publications concerning this thesis

1. *Well-ordered arranging of Ag nanoparticles in SiO_2/Si by ion implantation*

   K. Takahiro, Y. Minakuchi, K. Kawaguchi, T. Isshiki, K. Nishio, M. Sasase, S. Yamamoto, F. Nishiyama

   Appl. Surf. Sci. **258** (2012) 7322-7326

2. *Blue-shift and Narrowing of Localized Surface Plasmon Resonance of Silver Nanoparticles Exposed to Plasma*

   K.Kawaguchi, M. Saito, K. Takahiro, S. Yamamoto, M. Yoshikawa

   Plasmonics **6** (2011) 535-539

3. *Plasmonic cyclohexane-sensing by sputter-deposited Au nanoparticle array on SiO_2*

   K. Kawaguchi, S. Yamamoto, M. Yoshikawa, K. Takahiro

   to be published in Thin Solid Films

Publications concerning other studies

1. *Oxygen reduction activity of N-doped carbon-based films prepared by pulsed laser deposition*

   T. Hakoda, S. Yamamoto, K. Kawaguchi, T. Yamaki, T. Kobayashi, M. Yoshikawa

   Appl. Surf. Sci. **257** (2010) 1556-1561

International conference

1. *Modification of Ag Nanoparticles on SiO_2 Substrate by Ion Irradiation*

   K. Kawaguchi, K. Yoshimura, S. Yamamoto, M. Yoshikawa, K. Takahiro

   The 19th MRS-J Academic Symposium, Japan, 2009

2. *Sputtering and Plasma Exposure to Fabricate Gold Nanoparticles with Clean Surfaces*

   K. Kawaguchi, T. Sanari, K. Takahiro, S. Yamamoto, M. Yoshikawa, S. Nagata

   The 11th International Symposium on Sputtering & Plasma Processes, Japan, 2011

3. *OPTICAL PROPERTY OF GOLD NANOPARTICLES MODIFIED BY PLASMA EXPOSURE AND SPUTTERING*

   K. Kawaguchi, T. Sanari, K. Takahiro, S.Yamamoto, M.Yoshikawa, S. Nagata

   The 17th International Conference on Surface Modification of Materials by Ion Beam, China, 2011

4. *Optical Property of Gold Nanoparticles Modified by Plasma Exposure and Sputtering*

   K. Kawaguchi, T. Sanari, K. Takahiro, S.Yamamoto, M.Yoshikawa, S. Nagata

   The 18th International Conference on Ion Beam Modifications of Materials, China, 2012

5. *Blueshift and Narrowing of Localized Surface Plasmon Resonance of Au Nanoparticles Modified by Plasma and Ion Treatments*

   K. Kawaguchi, S. Yamamoto, M. Yoshikawa, K. Takahiro

   12th International Conference on Atomically Controlled Surfaces, Interfaces and Nanostructures, Japan, 2013

Acknowledgements

The author would like to express the deepest appreciation to Prof. Katsumi Takahiro made enormous contribution to this study. Without his guidance and continuing support, this thesis would not have been possible to complete.

A part of this work has been carried out during my stay in Takasaki Advanced Radiation Research Institute of Japan Atomic Energy Agency as a research student. The author greatly appreciates Dr. Masahito Yoshikawa providing me such an opportunity. I am grateful to Dr. Shunya Yamamoto for his sincere cooperation and concern over my work. I would like to express my gratitude to Dr. Teruyuki Hakoda and Dr. Tetsuya Yamaki for their valuable comments and suggestions concerning this work.

I would like to thank Prof. Toshiyuki Issiki for contribution on TEM observation. I appreciate all the member of Takahiro laboratory in Kyoto Institute of Technology for collaborating on my study.

Finally, I would like to express my special thanks to my father, mother, and sisters for tremendous support and sincere encouragement.

Kyoto

March 2014 Kazuhiro Kawaguchi